Riker, J. M., Blundy, J. D., Rust, A. C., Botcharnikov, R. E., & Humphreys, M. C. S. (2015). Experimental phase equilibria of a Mount St. Helens rhyodacite: A framework for interpreting crystallization paths in degassing silicic magmas. Contributions to Mineralogy and Petrology, 170, [6]. DOI: 10.1007/s00410-015-1160-5

Experimental phase equilibria of a Mount St. Helens rhyodacite: A framework for interpreting crystallization paths in degassing silicic magmas

Jenny M. Riker * · Jonathan D. Blundy · Alison C. Rust · Roman E. Botcharnikov · Madeleine C. S. Humphreys

J. Riker · J. Blundy · A. Rust
School of Earth Sciences, University of Bristol, Bristol, BS8 1RJ, United Kingdom

R. Botcharnikov
Institüt fur Mineralogie, Universität Leibniz Hannover, D–30167, Hannover, Germany

M. Humphreys
Department of Earth Sciences, Durham University, Durham, DH1 3LE, United Kingdom

* Corresponding author: Tel: +44 (0)117 331 5181. Fax: +44 (0)117 925 3385. Email: jenny.riker@bristol.ac.uk

Keywords:
Mount St. Helens · volatiles · CO_2 · magma degassing · crystallization · phase equilibria

Abstract

We present isothermal (885 °C) phase equilibrium experiments for a rhyodacite from Mount St. Helens (USA) at variable total pressure (25–457 MPa) and fluid composition (XH_2O^{fl} = 0.6–1.0) under relatively oxidizing conditions (NNO to NNO+3). Run products were characterized by SEM, electron microprobe, and SIMS. Experimental phase assemblages and phase chemistry are consistent with those of natural samples from Mount St. Helens from the last 4,000 years. Our results emphasize the importance of pressure and melt H_2O content in controlling phase proportions and compositions, showing how significant textural and compositional variability may be generated in the absence of mixing, cooling, or even decompression. Rather, variations in the bulk volatile content of magmas, and the potential for fluid migration relative to surrounding melts, mean that magmas may take varied trajectories through pressure–fluid composition space during storage, transport, and eruption. We introduce a novel method for projecting isothermal phase equilibria into CO_2–H_2O space (as conventionally done for melt inclusions) and use this projection to interpret petrological data from Mount St Helens dacites. By fitting the experimental data as empirical functions of melt water content, we show how different scenarios of isothermal magma degassing (e.g. water-saturated ascent, vapor-buffered ascent, vapor fluxing) can have quite different textural and chemical consequences. We explore how petrological data might be used to infer degassing paths of natural magmas and conclude that melt CO_2 content is a much more useful parameter in this regard than melt H_2O.

1 Introduction

Degassing and concomitant crystallization modulate the chemical and physical properties of erupting magmas, but direct evidence of the degassing behavior of arc magmas remains elusive. Instead petrologists rely on indirect methods to infer degassing processes, including petrography, textural analysis, mineral chemistry, melt inclusion analysis and thermodynamic modeling. In this paper we use experimental phase equilibria of a rhyodacite composition from Mount St. Helens, USA, as a framework for interpreting magma degassing paths.

H_2O and CO_2 are typically the most abundant volatile species in silica-rich arc magmas. Although H_2O predominates, water loss from magmas strongly depends on the abundance of

CO_2, which affects the partial pressures of both components. For this reason, solubility relationships and degassing paths are often represented on conventional plots of melt CO_2 vs. H_2O (e.g. Holloway and Blank 1994; Newman and Lowenstern 2002). In the idealized case of closed-system decompression, melts exsolve CO_2 in preference to H_2O until the late stages of degassing, when almost all CO_2 has been stripped from the melt. The resulting degassing trajectory in CO_2–H_2O space is strongly curved and runs oblique to "isopleths" of constant vapor composition. Alternate degassing scenarios may include open system degassing, whereby gas is continuously removed from the melt (Newman and Lowenstern 2002); degassing + crystallization, which concentrates H_2O in melt and vapor (e.g. Bundy and Cashman 2008); or "isobaric fluxing" of melt stored at shallow levels by gas released at depth (e.g., Blundy et al. 2010), which displaces melt towards more CO_2-rich compositions. Kinetic effects, related to variable volatile diffusivities through silicate melt (e.g. Gonnermann and Manga 2005), may further complicate degassing behavior. The reader is referred to Blundy and Cashman (2008) for a more detailed exploration of these scenarios.

Petrology paints an increasingly complex picture of degassing behavior in volcanic systems. In particular, the H_2O and CO_2 contents of melt inclusions rarely describe simple, closed-system degassing paths; rather, they define broad arrays suggestive of varied trajectories through H_2O–CO_2 space (Blundy et al. 2010). The compositions and textures of complexly zoned phenocrysts attest to the role of variable melt water content in the P–T–t evolution of crystallizing magmas (e.g., Rutherford and Devine 2008; Streck et al. 2008; Cashman and Blundy 2013). Constraints from diffusion chronometry suggest that such variations may occur on eruptive timescales (days to months, e.g. Saunders et al. 2012). It follows that crystals can preserve valuable information on the composition, quantity, and mobility of fluid in volcanic systems, and their relationship to discrete eruptive events. A key question is whether the degassing record from crystal compositions and textures can be reconciled with that from melt inclusions.

Experimental studies can help link the petrologic record to coupled processes of degassing and crystallization. Although many studies have investigated the solubility and partitioning of volatiles in magmas of varied composition (as reviewed by Baker and Alletti 2012), such studies are overwhelmingly focused on crystal-free systems. Phase equilibria investigations of crystal-bearing magmas incorporating multi-component fluids are generally aimed at replicating static pre-eruptive magma storage conditions (e.g., Blundy and Cashman 2008; Hammer 2008). Studies emphasizing the co-evolution of melt+fluid±crystals in response to degassing of multi-component fluids are rare and typically lack quantitative

information on fluid composition (e.g. Mangan and Sisson 2000; Cichy et al. 2011).

We present isothermal phase equilibria experiments in pressure–fluid composition space designed to assess the effect of degassing of binary H_2O–CO_2 fluids on the petrological evolution of crystallizing silicic magmas. These experiments emphasize the role of degassing path in controlling the compositions and textures of erupted products, showing how significant variability in phase assemblages, abundances, and compositions may be generated in the absence of magma mixing, cooling or heating, or even decompression. Rather, variations in the bulk volatile content of magmas, and the potential for fluid migration relative to surrounding melts, are capable of generating a wide range of petrographic characteristics. As a case study, we utilize the well-characterized Mount St. Helens (USA) volcanic system. Our run temperature (885 °C), pressures (25–457 MPa), and fluid compositions (60–100 mol% H_2O) are constrained by existing petrologic data, including Fe–Ti oxide thermometry (Blundy et al. 2008), melt inclusion volatile contents (Blundy et al. 2010; Cashman and Blundy 2013), and phase equilibria constraints on magma storage depths (Rutherford et al. 1985; Rutherford and Devine 1988; Gardner et al. 1995b). In this way, our run conditions simulate isothermal degassing of magma at depths ranging from the mid-crust to the near surface.

2 Experimental Methods

Our starting material is a synthetic equivalent of a natural rhyodacite (dome sample DS-63 of Smith and Leeman 1987) from the Sugar Bowl eruptive sequence of Mount St. Helens (1200 y.b.p.; Mullineaux 1986). This rhyodacite is the most felsic composition erupted at Mount St. Helens in the past 4,000 years, with bulk compositions sitting at the intersection of whole rock and melt inclusion major element trends (Blundy et al. 2008). As such, these lavas are unlikely to have been significantly modified by processes of magma mixing and crystal accumulation that have been documented in previous petrologic studies (Gardner et al. 1995a; Heliker 1995; Berlo et al. 2007; Cashman and Blundy 2013). We take this rhyodacite composition to be broadly representative of the reactive liquid portion of the volcano's shallow magmatic system, and our experiments are chemically 'scaled' (in the sense of Pichavant et al. 2007) to simulate the evolution of this melt to produce phenocryst rims and groundmass (i.e., the subsystem in local chemical equilibrium on the timescales of processes being investigated). Although the Sugar Bowl rhyodacite itself may not have experienced the diversity of degassing trajectories simulated in this study, our aim is to make general

inferences regarding degassing processes that may be relevant to Mount St. Helens and other dacitic arc volcanoes.

Volatile-free (SB3) and CO_2-bearing (SB4) starting materials for experiments were prepared as mechanical mixtures of reagent grade oxides and carbonates. Mixtures were repeatedly fused under gas-buffered conditions (NNO+1) to yield homogeneous glass powders; see supplementary materials for details. Compositions of SB3 and SB4 are given in Table 1. As we aim to investigate processes driven by degassing and decompression, our experiments were isothermal, at a temperature (885 °C) chosen to match that of pre-eruptive magma storage prior the 1980–1986 eruptions of Mount St. Helens (875–900 °C; Blundy et al. 2008).

All experiments were run saturated with either a pure-H_2O or H_2O–CO_2 fluid. In water-only experiments ($P_{total} = P_{H2O}$), volatile-free starting material was loaded into Au capsules along with sufficient water to saturate the charge at run conditions (as estimated following Papale et al. 2006). Capsules were sealed shut with a micro-welder, heated briefly (>100 °C), and re-weighed to verify the integrity of the weld prior to running. Following each run, capsules were weighed again to check for loss or gain of components. The presence of excess water was verified visually on piercing, or by weight loss on heating (samples with anticipated dissolved water contents > ~6 wt% were not heated to avoid diffusive loss of H_2O; see Holtz et al. 1992). Water pressure (P_{H2O}) less than total pressure ($P_{total} = P_{H2O} + P_{CO2}$) was achieved by addition of water to carbonated starting powder (SB4; Table 1); in a subset of runs (n = 5), carbon was added to volatile-free starting material as $Ag_2C_2O_4$, which decomposes to Ag + CO_2 above 140 °C. The amount of water added was then varied to achieve the target H_2O–CO_2 fluid composition (after Papale et al. 2006). Vapor saturation of CO_2-bearing charges could not always be confirmed by piercing or heating, as the masses of excess fluid were small (e.g., Burnham and Jahns 1962). Nevertheless, the amount of CO_2 added exceeds by several thousand ppm that expected to dissolve in the melt at run conditions (Newman and Lowenstern 2002; Papale et al. 2006).

Experiments at P_{total} <250 MPa were run in externally-heated cold seal Nimonic pressure vessels at the University of Bristol (excepting DSB6, run on an identical apparatus at the University of Oregon) with water as the pressurizing medium. Typically, 2-3 charges of different fluid composition were loaded simultaneously to minimize inter-run variations in P and T. Pressure was monitored on digital transducers or Heise gauges and controlled to within 1 MPa of the target value. Temperature was monitored using K-type thermocouples accurate to ±3 °C. Samples were positioned in the furnace hot spot, where thermal gradients

were <2-3 °C over the capsule length (<1 cm). At the end of each run, charges were rapidly quenched by lowering the magnetic sample holder into the water-cooled "cold seal" at the vessel base. An additional six experiments (P_{total} ≥350 MPa) were run in internally-heated pressure vessels (IHPV) at Leibniz Universität Hannover, pressurized using an Ar–H_2 gas mixture. Temperature was measured using four thermocouples positioned along the 30 mm hot zone of the sample holder; gradients were <5 °C across the capsule length. Charges were suspended from Pt wire and drop-quenched at the end of each run. Run times ranged from 48 to 506 hours, depending on pressure and fluid composition. Chips of quenched run products were mounted in resin, ground and polished, and analyzed for major elements and volatiles as described in the supplementary materials.

The oxygen fugacity of IHPV runs was maintained near the NNO buffer (Table 2) by controlling the proportions of Ar and H_2 in the pressurizing gas, monitored through use of an H_2-permeable membrane adjacent to the sample holder (Berndt et al. 2002). The oxygen fugacity of cold-seal experiments was not buffered, but several experiments generated co-existing oxides that indicate fO_2 of 2.3–3.4 log units above the NNO buffer (Lepage 2003; Table 2). These conditions are more oxidizing than those inferred for the Pine Creek and Kalama tephras (NNO+1.3–1.4; Gardner et al. 1995b), which chronologically bracket the Sugar Bowl lavas; however, similar conditions have existed among earlier erupted dacites at Mount St. Helens (Smith Creek period, NNO+2.2–2.7; Gardner et al. 1995b). We do not consider this offset to have major implications for phase stability in our runs, but it should be borne in mind when examining phase compositions of mafic minerals.

3 Results

3.1 Run products

Run conditions and phase assemblages of 29 experimental charges are summarized in Table 2. Runs are isothermal (885 °C), with pressures ranging from 25 to 457 MPa and calculated fluid compositions (XH_2O^{fl}, Sec. 3.2) between 0.6 and 1.0. All run products are well-quenched, bubbly glasses containing crystals of plagioclase, amphibole, pyroxenes, and/or Fe–Ti oxides. Crystalline phases are homogeneously distributed throughout each charge and are typically euhedral to elongate, with the exception of plagioclase, whose habits become increasingly skeletal or chain-like at low pressures and low XH_2O^{fl} (Fig. 1). Phases were identified primarily by EPMA and semi-quantitative EDS, with positive identification of

small or rare phases aided by observations of crystal habit; for example, rhombohedral oxides could be readily distinguished from magnetite by their tabular shapes (Fig. 1c).

Our starting material is a glass powder, and equilibration of each run proceeded by the nucleation and growth of crystals from melt ('crystallization experiments'; e.g., Holtz et al. 1992). We have not performed melting experiments to demonstrate reversibility, because the small size of crystals (often < 5 μm) would preclude the analysis of crystal rims in such runs. However, several lines of evidence attest to the attainment of equilibrium in our sample suite: (a) run durations equivalent to (or longer than) equilibration times demonstrated by reversals in previous studies of silica-rich magmas at similar conditions (e.g., Gardner et al. 1995b; Hammer et al. 2002; Castro and Dingwell 2009); (b) the uniform distribution and size of crystalline phases within each charge, suggesting ease of nucleation; and (c) the low residuals of mass balance calculations (almost always <0.1; supplementary materials). Mineral–melt exchange coefficients for plagioclase ($K_D = (Ca/Na)_{plag}/(Ca/Na)_{liq}$) are within the range reported in other experimental studies of hydrous silicic melts (2.4–4.4; compared to 3.1–6.9, Gardner et al. 1995b; 1.8–3.9, Scaillet and Evans, 1999; 2.0–7.2, Sisson et al. 2005; and 3.0–8.0, Martel 2012) and positively correlated with indices of melt evolution, as expected for equilibrium crystallization of plagioclase (e.g., Sisson et al. 2005). Moreover, 70% of runs give plagioclase–melt thermometry temperatures within 50 °C of known run temperatures, as calculated using the equilibrium algorithm of Putirka (2008, equation 24a). K_D (= $(Fe^{2+}/Mg)_{min}/(Fe^{2+}/Mg)_{liq}$) of mafic phases are less straightforward indicators of equilibrium given their sensitivity to redox state, and $Fe^{3+}/\Sigma Fe$ ratios of melt and minerals are not known for most samples. However, K_D calculated for two pyroxene-bearing runs in which glasses were directly analyzed for Fe^{2+} and Fe^{3+} by μXANES are consistent with the accepted equilibrium value of 0.3 (Putirka 2008). Calculated K_D are reported in the supplementary materials.

3.2 Volatile concentrations

Dissolved volatiles The dissolved H_2O concentrations of experimental glasses range from 3.2–9.8 wt% (Table 2). Water contents likely extend to lower values but could not be measured in a single low-pressure run (PSB28) due to its high crystallinity; the value reported for this sample is a modeled water solubility (Table 2; Papale et al. 2006). SIMS measurements agree well with H_2O contents estimated "by difference" from EPMA analyses (75% agree within uncertainty; see supplementary materials), and the absolute average

deviation of the two data sets is 0.49 wt% (better than the propagated precision of by-difference values). Scatter is greater at high water contents, where the precision of both techniques may be affected by the instability of water-rich rhyolite glasses (e.g., Ihinger et al. 1994; Devine et al. 1995; Hauri et al. 2002). As expected, dissolved H_2O concentrations show a pronounced pressure dependence (Fig. 2a), decreasing, at water-saturated conditions, from 9.8 wt% to 3.2 wt% between 457 and 50 MPa. The addition of CO_2 decreases H_2O fugacity (e.g., Blank et al. 1993; Dixon et al. 1995) such that H_2O contents decrease at constant total fluid pressure (P_{total}) with increasing CO_2 content (Fig. 2c). Dissolved CO_2 concentrations range from below detection (26 ppm) to 2325 ppm and are highest in mixed fluid runs at P = 457 MPa (Fig. 2b). CO_2 concentrations decrease dramatically with decreasing P_{total} at high pressures. In water-saturated runs, CO_2 contents are just above detection limits, indicating minimal carbon contamination of starting materials.

Fluid composition Fluid composition is a key intensive variable in our experimental suite. Throughout this paper, we report fluid composition as the mole fraction of water, XH_2O^{fl}, in a binary H_2O–CO_2 fluid phase, assuming other components (e.g., N_2 from trapped air; dissolved silicates) contribute negligibly to the total fluid pressure. There are several approaches to estimating the fluid composition of experimental run products: the mass ratio of exsolved H_2O and CO_2 may be measured gravimetrically (e.g., Tamic et al. 2001), calculated by mass balance from known bulk and dissolved volatile concentrations (e.g., Lesne et al. 2011), or estimated using solubility or partitioning models (e.g., Gardner et al. 1995b; Hammer et al. 2002). In our runs, the small volume of free fluid did not permit accurate determination of XH_2O^{fl} by gravimetry, while mass balance calculations incorporate a large number of variables and associated uncertainties that yield unacceptably large errors (often >20% relative). We instead calculate fluid compositions from measured H_2O and CO_2 concentrations using the compositionally-dependent solubility model of Papale et al. (2006). This approach yields a self-consistent set of values derived from well-constrained variables: run temperature, dissolved volatile concentrations, and measured glass compositions. It also encompasses sources of uncertainty that are not easily constrained (e.g., weighing errors or adsorption of H and C onto starting powders). Fluid compositions estimated in this way are largely indistinguishable from those estimated by mass balance within the relatively large error of the latter.

Calculated XH_2O^{fl} are between 0.6 and 1.0 (Table 2). These values rely critically on the solubility model used; to justify our choice, Fig. 3 compares known experimental pressures to

saturation pressures calculated using Papale et al. (2006) and using VolatileCalc (Newman and Lowenstern 2002). Measured H_2O and CO_2 contents are also compared to isobars and vapor isopleths calculated after Papale et al (2006) in Fig. 2c. Although both models tend to overestimate known run pressures, the model of Papale et al. (2006) better replicates run pressures across the entire investigated pressure range. In contrast, saturation pressures calculated using VolatileCalc deviate strongly from known values at pressures >250 MPa. Comparison of experimental data with model predictions suggests our approach may introduce an additional, systematic uncertainty in calculated fluid compositions (Fig. 2c), but this is unlikely to be greater than the error in mass balance calculations.

3.3 Phase relations in P–XH_2O^{fl} space

Isothermal phase relations for the Sugar Bowl rhyodacite depend strongly on pressure and fluid composition (Fig. 4). Similar relationships are observed in other experimental studies of natural magmatic systems (e.g. Rutherford et al. 1985; Rutherford and Devine 1988; Gardner et al. 1995b; Scaillet and Evans 1999; Hammer et al. 2002; Pichavant et al. 2002; Scaillet et al. 2008) and underscore the role of water, which has highly pressure-dependent solubility, in influencing the stabilities of hydrous and anhydrous minerals (e.g. Tuttle and Bowen 1958; Ebadi and Johannes 1991; Holtz et al. 1992).

Titanomagnetite is the liquidus phase at our run temperature and is observed in all run products (Table 2; Fig. 4). At lower pressures, plagioclase joins the stable assemblage, followed by orthopyroxene, except at the most water-rich fluid compositions ($XH_2O^{fl} \approx 1$), where the amphibole-in curve crosses the plagioclase and pyroxene phase boundaries. The isothermal saturation pressures of all anhydrous phases increase with decreasing XH_2O^{fl}. In contrast, amphibole stability is greatly reduced at lower melt water contents, as reflected by the pronounced curvature of the saturation surface in P-XH_2O^{fl} space. The low-pressure bound of the amphibole saturation surface is coincident with melt water contents of ~4 wt% (Fig. 4), an approximate lower limit of amphibole stability in hydrous melts (Eggler and Burnham 1973; Ridolfi and Renzulli 2012). The high-pressure limit of the isothermal amphibole stability curve is constrained by the absence of amphibole at 225 MPa and water-saturated conditions, and for $XH_2O^{fl} < 0.7$ amphibole is not stable at any pressure.

Rhombohedral oxides have irregular stability in our experimental suite, and the two-oxide stability field is poorly-constrained. This suggests that we are near the saturation surface of rhombohedral oxides, in keeping with previous experimental studies of Mount St.

Helens dacites that find oxide stability to be strongly dependent on temperature and oxygen fugacity (Rutherford et al. 1985; Rutherford and Devine 1988; Gardner et al. 1995b). Discrepancies may therefore be attributable to temperature uncertainties, or to a slight reduction of fO_2 with decreasing water activity, a consequence of the coupling of the imposed fH_2 to the fH_2O and fO_2 in the charge (e.g., Scaillet and Evans 1999; Sisson et al. 2005). This effect is seen in the calculated oxygen fugacities of run products at identical P and T (Table 2), which decrease systematically as XH_2O^{fl} decreases.

A silica phase and apatite are found in a small number of experimental samples. Silica occurs as isolated crystals (sample PSB54) and as an anhedral phase that appears to partially or wholly infill vesicles (sample PSB28), consistent with the identification of silica polymorphs (tridymite and cristobalite) in dome samples from recent eruptions of Mount St. Helens (Hoblitt and Harmon 1993; Blundy and Cashman 2001; Pallister et al. 2008). The presence of silica at P_{total} = 150 MPa suggests that low pressure crystallization is not required for silica saturation (as posited by Blundy and Cashman 2001), as long as melt H_2O content is sufficiently low. Rare skeletal apatite crystals are observed in two low-pressure, water-saturated runs, and our phase boundary is drawn to reflect this narrow stability field.

Equilibrium experiments identify five major stable phases (plag, amph, opx, magnetite, and ilmenite) that are consistent with mineral assemblages observed in previous experimental studies of dacitic phase equilibria at Mount St. Helens (Merzbacher and Eggler 1984; Rutherford et al. 1985; Rutherford and Devine 1988; Geschwind and Rutherford 1992; Rutherford and Hill 1993; Gardner et al. 1995b; Rutherford and Devine 2008). This same assemblage is broadly characteristic of dacites erupted at the volcano over the past 4000 years (Halliday et al. 1983; Mullineaux 1986; Smith and Leeman 1987; Pallister et al. 1992; Gardner et al. 1995a), with the exception of cummingtonite, found in the Smith Creek tephras (Smith and Leeman 1987; Gardner et al. 1995a) and reproduced in the relatively cool (<800°C) experiments of Geschwind and Rutherford (1992). Although trace abundances of augite are found in some natural dacites and produced in minor quantities in experiments (Merzbacher and Eggler 1984; Rutherford et al. 1985; Rutherford and Devine 1988; Rutherford and Devine 2008), augite is absent from both the Sugar Bowl dome rhyodacite (Smith, 1984; Smith and Leeman, 1987) and our experiments.

3.4 Crystallinity and phase proportions

Phase abundances have been calculated from measured bulk, glass, and mineral compositions

(on an anhydrous basis) using least-squares regression (supplementary materials). Residuals of mass balance calculations are generally low ($\Sigma r^2 \leq 0.05$ in all but three runs), and the standard error on regression coefficients is always <2 wt% absolute, suggesting that analytical sodium loss is minimal even in very hydrous glasses. For a single sample lacking glass analyses, we have estimated phase proportions by point counting representative BSE images (see supplementary materials for details). We have also point-counted two near-liquidus samples for which mass balance calculations give low crystal fractions inconsistent with visual estimates (probably a result of large relative errors in mass balance estimates at very low crystal contents).

Calculated phase abundances illustrate several key aspects of the crystallizing system. First, as expected, total crystallinity increases dramatically with decreasing pressure (at constant temperature and XH_2O^{fl} ; Fig. 5a) and with decreasing XH_2O^{fl} (at constant pressure; Fig. 5b). Second, plagioclase is by far the most abundant crystallizing phase in our sample suite, except at high pressures, where crystallinities are low and orthopyroxene abundance equals or exceeds that of plagioclase. This shift in relative abundances could indicate the convergence or crossing of the plagioclase and orthopyroxene liquidi within our phase diagram (as observed in the experiments of Merzbacher and Eggler 1984 and Rutherford et al. 1985), although the location of this transition cannot be resolved from the observed phase assemblages (Table 2). Plagioclase crystallinities in experimental run products range from trace quantities near the liquidus to 51 wt% at the lowest P_{total} investigated; the mass fractions of all other mineral phases remain comparatively low (<5 wt%). The predominance of plagioclase across much of the investigated parameter space is consistent with its ubiquity as a phenocryst and groundmass phase in natural dacites (e.g., Smith and Leeman 1987; Gardner et al. 1995a).

3.5 Phase compositions

Glass compositions Major element compositions of experimental glasses (supplementary materials) range from rhyodacitic to rhyolitic and become increasingly evolved (higher SiO_2 and K_2O, lower Al_2O_3, CaO, FeO_T, and MgO) at lower pressures and water-poor fluid compositions, reflecting progressive, isothermal crystallization with decreasing pressure (at constant fluid composition) and/or decreasing XH_2O^{fl} (at constant pressure). Experimental glass compositions overlap with those of natural groundmass and melt inclusion glasses from the 1980–1986 and 2004–2008 eruptions of Mount St. Helens (Fig. 6) and encompass nearly

the entire range of glass SiO_2 contents generated during this activity (Blundy et al. 2008). These data lend support to our choice of starting composition and emphasize the ability of polybaric, volatile-driven crystallization, in the absence of any cooling, to generate much of the compositional diversity observed in silica-rich volcanic glasses (e.g. Cashman 1992; Blundy and Cashman 2001). Slight offsets between the Al_2O_3 and CaO contents of experimental and natural glasses probably reflect minor differences in bulk composition.

A pronounced feature of Fig. 6 is the offset between the Na_2O contents of natural versus experimental glasses. Experimental glasses extend smoothly from the whole rock trend before decreasing at higher silica contents, while natural glasses show a pronounced inflection to the whole rock data. This mismatch is unlikely to be an analytical effect (Sec. 3.4). Blundy et al. (2008) have previously attributed the inflection observed in natural samples to the onset of volatile-saturated crystallization, during which Na partitions preferentially into vapor. It is possible that our experiments became vapor saturated at less evolved (lower SiO_2) compositions than the natural glasses (perhaps due to higher bulk water contents in experiments compared to the natural system), preventing melt Na contents from rising to values seen in erupted products. Higher experimental bulk water contents would lead to more Na_2O being sequestered by the vapor phase throughout the crystallization interval; in natural magmas, exsolved vapor fractions during crystallization would be comparatively low. In this way, volatile elements (e.g., Na, K) have the potential to provide a useful marker of the presence and abundance of vapor in a magmatic system.

Mineral compositions Experimentally-generated plagioclase compositions (mol% anorthite) range from An_{52} near the plagioclase liquidus to An_{32} (supplementary materials); compositions may extend to more albitic values but could not be analyzed in one low-pressure sample. Fig. 7a compares measured An contents to published plagioclase compositions for natural Mount St. Helens dacites erupted over the past 4000 years, which display a remarkably broad compositional range (An_{82}–An_{17}; Smith 1984; Smith and Leeman 1987; Cashman 1992; Gardner et al. 1995a; Cooper and Reid 2003; Berlo et al. 2007; Streck et al. 2008). Our experimental plagioclase fall at the sodic end of this range and are compositionally equivalent to those found in the Sugar Bowl lavas (An_{50}–An_{32}; Smith 1984; Smith and Leeman 1987; Berlo et al. 2007). Experimental plagioclase compositions also overlap with those of microphenocrysts and phenocryst rims from the 1980–1986 and 2004–2008 eruptive episodes (An_{54}–An_{30}; Cashman 1992; Streck et al. 2008). Most authors interpret highly calcic values (>An_{60}) as xenocrystic or antecrystic cores; the more limited

compositional range (~An_{50}–An_{30}) is probably typical of plagioclase grown from dacitic melts. While most compositions fall close to the An-Ab binary, a small increase in the orthoclase component is observed at An <40 mol% (up to Or_3; Fig. 7a).

Although temperature exerts a primary control on plagioclase composition (Rutherford et al. 1985; Gardner et al. 1995b; Cashman and Blundy 2013), the subsidiary effect of melt water content is also important, and numerous experimental studies have shown that plagioclase becomes more albitic as P_{H2O} decreases at constant temperature (Rutherford et al. 1985; Rutherford and Devine 1988; Gardner et al. 1995b; Hammer et al. 2002; Couch et al. 2003; Moore 2008; Brugger and Hammer 2010; Martel 2012). This effect is illustrated in Fig. 7 for subsets of water-saturated (Fig. 7b) and isobaric runs (Fig. 7c), which trend towards more sodic compositions with decreasing pressure and XH_2O^{fl}, respectively. The magnitude of the isothermal pressure dependence of anorthite content can be described by a simple linear fit to the water-saturated dataset, which yields a decrease of 5 mol% An for every 50 MPa drop in P_{total} (a comparable change through isobaric cooling requires a drop of ~14°C; Cashman and Blundy 2013). A similar fit to the isobaric data suggests that XH_2O^{fl} must decrease by 0.1 to produce the same change in plagioclase composition at 200 MPa. These fits are approximate, as our data do not extend to low pressures and water-poor fluid compositions, where An contents should approach the solidus composition.

Fe–Ti oxides occur as both cubic and rhombohedral varieties in our experiments. Rhombohedral oxides are found in just ten runs, with compositions falling on the Ti-poor side of the ilmenite–hematite solid solution (Ilm_{24}–Ilm_{44}, calculated after Stormer 1983; supplementary materials). Where possible, the oxygen fugacities of run products have been calculated from co-existing oxides using ILMAT (Lepage 2003); these calculations yield relatively oxidizing fO_2 of NNO+2.3–3.4 (Table 2). The Usp contents of titanomagnetite span a wide range (Usp_4–Usp_{45}; supplementary materials) and are strongly clustered, such that the TiO_2 contents of cubic and rhombohedral oxides in our sample suite overlap. Where only one oxide is present, it is assumed to be ülvospinel, consistent with inferences based on crystal habit.

In contrast to plagioclase, the compositions of mafic phases (amphibole, orthopyroxene, and Fe–Ti oxides; see supplementary materials) show no clear variation with water content in our runs. Amphibole crystals could be analyzed in only three charges, and no systematics emerge from this small dataset. Orthopyroxenes span a range of endmember compositions (En_{56}–En_{84}), with wollastonite contents of 1–2 mol% in all but two high-pressure runs (Wo_3–Wo_4, perhaps due to low plagioclase abundance in these charges).

Orthopyroxene compositions overlap with those for natural Mount St. Helens dacites spanning the last 13,000 years of activity (En_{52}–En_{73}; Smith 1984; Smith and Leeman 1987; Saunders et al. 2012) but extend to higher En and Mg# (Fig. 8a). The range of pyroxene compositions cannot be attributed to temperature in our runs, although temperature may be partly responsible for compositional variability in natural pyroxenes. A more likely cause of the compositional shifts observed in experiments are variations in fO_2 (e.g. Rutherford and Devine 1988; Scaillet and Evans 1999), which affect the amount of ferrous iron in the melt available for incorporation into orthopyroxene. Orthopyroxene compositions are broadly correlated with the oxygen fugacities reported in Table 2 (Fig. 8b) and with the TiO_2 content of co-existing magnetite.

To corroborate oxygen fugacities estimated from oxide compositions, the glassiest run products (n = 8) were analyzed for Fe^{2+} and Fe^{3+} by μXANES (Table 2; see supplementary materials for analytical methods). For charges with $XH_2O^{fl} \approx 1$, values of ΔNNO inferred from μXANES (+0.9 to +2.7) overlap with those estimated from oxide compositions (+2.3 to +3.4). CSPV runs span the range of measured fO_2 values, while IHPV runs fall at the low end of this range, reflecting the fact that IHPV runs were maintained at more reducing conditions via H_2 in the pressurizing gas. Given the abundance of plagioclase in our experimental system, variations in run fO_2 should not strongly influence the systematics of other variables considered here (e.g. crystallinities, plagioclase compositions, and glass compositions, with the exception of FeO_T).

4 Discussion

Our results reinforce the findings of many previous experimental investigations that have shown crystal–melt equilibria to be strongly dependent on dissolved water content. Furthermore, the isothermal and isochemical nature of our experiments has allowed us to demonstrate how changes in melt H_2O concentration, driven solely by changes in pressure and fluid composition, are capable of generating rocks with a wide range of petrographic and petrologic characteristics. In the case of the Sugar Bowl rhyodacite, this range encompasses much of the compositional diversity observed in groundmass ± microlites ± crystal rims in the felsic erupted products of Mount St. Helens. This observation is important, emphasizing that mixing of magmas of significantly different compositions and/or temperatures is not required to explain the range of textural and compositional variability found in silicic arc magmas (although such mixing certainly occurs; e.g., Gardner et al. 1995a; Heliker 1995;

Berlo et al. 2007; Cashman and Blundy 2013). Rather, variations in the bulk volatile content of magmas, and the potential for fluid migration relative to surrounding melts, mean that magmas may take varied trajectories through pressure–fluid composition space during storage, transport, and eruption. Our experiments afford a general framework for understanding the petrological consequences of these different ascent and degassing trajectories. In the following discussion we emphasize ways of representing experimentally-determined phase equilibria to foster interpretation of natural volcanic rocks.

Our approach employs isothermal phase relations; in natural magmatic systems, however, temperature may vary both within and between eruptions (as documented at Mount St. Helens and attributed to processes such as mixing, latent heating, or protracted shallow storage; Blundy and Cashman 2005; Blundy et al. 2006; Blundy et al. 2008; Cashman and Blundy 2013). Phase relations are demonstrably sensitive to such variations (e.g., Rutherford et al. 1985; Rutherford and Devine 1988; Rutherford et al. 2008). Although considering the isothermal case allows us to isolate the importance of degassing processes, our approach could be augmented by extending the current experiments into temperature space. Kinetic effects may also impact on the evolution of crystal textures and compositions and are considered in a companion study (Riker et al. in review).

Several methods of portraying isothermal phase relations have been employed in the petrologic literature. The most common approach is to present phase relations in pressure–fluid composition space, as we have done above (Gardner et al. 1995b; Hammer and Rutherford 2002; Scaillet et al. 2008; Blundy et al. 2010). This approach has its limitations; frequently only bulk proportions of volatile components are reported, but these may deviate strongly from equilibrium fluid compositions at low fluid fractions. Fluid compositions are rarely directly measured or calculated by mass balance; when they are, uncertainties are typically large (>20% relative; e.g. Lesne et al. 2011). Integration of petrologic data from natural samples with those from experiments further requires independent knowledge of P and/or XH_2O^{fl}. An alternative approach is to construct phase diagrams using melt water content, rather than fluid composition, as an independent variable (P–H_2O diagrams, e.g. Di Carlo et al. 2006; Pichavant et al. 2009; or more commonly T–H_2O diagrams, e.g. Holtz et al. 2005; Botcharnikov et al. 2008). Water contents are often precisely known, thereby linking phase relations to a parameter that can be measured in erupted products. However, these projections tend to obscure the presence of CO_2 in the magmatic system; as such, they provide limited information on degassing trajectories. Here we consider a novel method of projecting phase relations and related information onto CO_2–H_2O diagrams, more commonly

used to portray melt inclusion data and modeled melt–vapor equilibria (e.g., Newman and Lowenstern 2002). As we will show, this type of projection enables the integration of petrologic data for magmatic processes that are more isothermal than isobaric. In this way, our experimental data present a useful context for interpreting the petrologic "fingerprint" of near-isothermal degassing in crystallizing magmas.

4.1 Modeling crystallization in CO_2–H_2O space

At fixed temperature and bulk composition, a degassing magma will take a path through CO_2–H_2O space that depends on the abundance, quantity, and mobility of fluids within the volcanic system and the extent to which equilibrium between melt, crystals, and vapor is maintained. We can explore the equilibrium case using a schematic CO_2–H_2O diagram, onto which we have projected our experimental phase boundaries as defined by measured glass volatile contents (Fig. 9). Additionally we show four endmember degassing trajectories (paths A–D in Fig. 9), calculated for our experimental composition after Papale et al. (2006). A simple linear correction has been applied to modeled saturation pressures to account for the offset with known run pressures ($P_{model} = 1.20 \times P_{experiment}$, $r^2 = 0.93$; Fig. 3a).

Each arrow in Fig. 9 is an isothermal degassing path capable of driving crystallization via melt dehydration. With the exception of the water-saturated case, all of these paths pass through the pressure (200 MPa) and assemblage (melt + vapor + oxides + plagioclase + amphibole + orthopyroxene) inferred for the top of the pre-1980 magma storage region. As such they represent plausible degassing scenarios capable of generating recent erupted products of Mount St. Helens. Path A shows an idealized, water-saturated degassing trajectory, whereby magma ascends in equilibrium with a pure-H_2O fluid, as commonly simulated in models and experiments. A more geologically plausible scenario is represented by Path B, a conventional closed-system degassing path (modeled for a nominal Mount St. Helens melt inclusion; see Fig. 9), in which fluid exsolved during ascent remains in equilibrium with surrounding melt. The strongly curved shape of this path reflects the low solubility of CO_2 compared to H_2O, assuming no excess fluid is present at the onset of decompression. If instead excess fluid is abundant, it may buffer the melt towards more CO_2-rich compositions (e.g., Rust et al. 2004; Blundy et al. 2010) yielding, in the extreme case of infinite vapor, a "vapor-buffered" trajectory along an isopleth of constant XH_2O^{fl} (Path C, $XH_2O^{fl} = 0.8$). Finally, Path D considers an initially CO_2-poor magma equilibrated with an increasingly CO_2-rich fluid (perhaps supplied from the deeper magmatic system) at a

constant pressure of 200 MPa. In this case, melt and gas exchange volatiles in a process called gas "fluxing" or "flushing" (e.g., Hammer and Rutherford 2003; Johnson et al. 2008; Blundy et al. 2010); as XH_2O^{fl} decreases, the dissolved water content of the melt decreases in tandem, such that gas is released.

Fig. 9 makes clear that magmas degassing according to these endmember scenarios will traverse different regions of phase stability. As such, they may be expected to record distinct petrologic signatures, reflected not only in phase assemblages, but also phase proportions, phase compositions, and crystallization sequences. What we would like to know is how these parameters vary along each degassing path, and how we might use this information to interpret processes of coupled degassing and crystallization in natural volcanic rocks.

In order to link our experimental data to the petrologic attributes of the Sugar Bowl rhyodacite, we need to quantify key parameters in terms of changing intensive variables. Fig. 10a shows the strong correlation between total crystallinity and measured melt water content, in keeping with the relationships described in Sec. 3.4. This correlation can be used to parameterize crystallinity as a hyperbolic[1] function of dissolved H_2O concentration:

$$\text{Crystallinity} = 32.1 - 9.66\ [\sinh (0.783 \times H_2O - 3.36)]\ (r^2 = 0.87, \textit{aad} = 4.2) \quad (3)$$

where crystallinity and H_2O are in wt% and *aad* is the average absolute deviation of data from model predictions. To extend our parameterization to the solidus, we have forced fits through experimentally-determined solidus water contents for the Qz–Ab–Or–H_2O–CO_2 system at XH_2O^{fl} = 0–1 (Ebadi and Johannes 1991). The water content of a single low-pressure run that could not be measured is constrained from the volatile-by-difference contents of long-duration (i.e. equilibrium) decompression experiments at the same terminal pressure (Riker et al. in review).

The same approach may be extended to individual phases and major melt components whose abundances depend to varying degrees on H_2O content, or on crystal–melt equilibria, themselves strongly controlled by H_2O content (Fig. 10). Regression of experimental data yields the following relations for mineral abundances and melt composition:

$$\text{Plagioclase (wt\%)} = 32.6 + 14.3\ [\sinh (-0.520 \times H_2O + 1.96)]\ (r^2 = 0.84, \textit{aad} = 4.0) \quad (4)$$

[1] We have used hyperbolic functions as they better describe the tendency of the experimental data to asymptote at high or low values without the arbitrary inflexion point that bedevils more commonly-used third-order polynomial fits.

Orthopyroxene (wt%) = 1.33 + 1.22 [sinh (– 0.641 × H_2O + 3.00)] (r^2 = 0.74, *aad* = 0.6) (5)

Fe-Ti oxides (wt%) = 1.09 + 0.99 [tanh (– 1.43 × H_2O + 9.19)] (r^2 = 0.56, *aad* = 0.5) (6)

SiO_2 in melt (wt%) = 73.6 – 4.70 [tanh (– 0.643 × H_2O + 3.60)] (r^2 = 0.83, *aad* = 1.0) (7)

Amphibole modes are low (<1.5 wt%, often trace) with large relative errors (supplementary materials), and for simplicity, we assume a constant amphibole abundance of 1 wt% within the amphibole stability field (and 0 wt% outside) in the illustrations that follow.

Plagioclase compositions are highly dependent on water concentrations (Sec 3.5). In our run products, however, anorthite content is more closely correlated with sample crystallinity (Fig. 10b), a consequence of the associated effect of melt composition:

An (mol%) = 43.7 + 18.0 [tanh (–0.0293 × crystallinity – 0.555)] (r^2 = 0.94, a.a.d = 1.1) (8)

where crystallinity is in wt%. Here we infer the solidus plagioclase composition (An_{26}) from the normative anorthite and albite contents of the bulk starting material. Equation 5 is used along with equation 4 to recast anorthite content in terms of dissolved water concentration. Similar expressions for mafic mineral compositions are not easily derived due to variations in run fO_2, and we do not consider them here.

Our parameterizations of the experimental data enable us to express key petrologic variables as functions of dissolved water content. Along with Fig. 9, these relationships constitute a simple, empirical model for describing the isothermal magmatic evolution of the Sugar Bowl rhyodacite with respect to changing melt H_2O and CO_2 concentrations. From these data, we may specify the attributes of co-evolving melt, vapor, and crystals at any point within our experimental parameter space.

4.2 Interpreting degassing paths in crystallizing magmas

For each of the degassing scenarios outlined above we can use our model to show how phase assemblages, compositions and abundances, and crystallization sequences vary during progressive isothermal degassing. This information is summarized in Figures 11a–d, which display phase proportions and equilibrium plagioclase compositions at discrete points along

each degassing path. Figures 11e–h additionally show how melt CO_2 and SiO_2 content, plagioclase composition, and total crystallinity vary as a function of total pressures ≤300 MPa.

Water-saturated ascent (Scenario A) During water-saturated ascent, only melt + minor oxides are stable at the onset of decompression (300 MPa, Fig. 11a). As pressure and melt water content decrease, first amphibole, then plagioclase begins to crystallize. The modeled plagioclase liquidus composition, An_{53}, is in good agreement with the most calcic groundmass crystals found in products of recent eruptions (An_{54}, Cashman 1992; Streck et al. 2008) and with calcic phenocrysts from the Sugar Bowl dome (An_{50}, Smith 1985; Smith and Leeman 1987). Below 200 MPa, orthopyroxene and trace apatite join the crystallizing assemblage; amphibole is no longer stable by 100 MPa and begins to break down. The initially crystal-free melt now contains 30 wt% crystals, dominated by plagioclase (An_{38}) with minor opx, oxides, and resorbing (or relict) amphibole. The melt continues to crystallize increasingly sodic feldspar during further decompression, and total crystallinity doubles to 61 wt% by 25 MPa. The melt becomes silica-saturated and, if crystallization proceeds at equilibrium, intersects the solidus at still lower pressures and water contents (in practice, this may be difficult to achieve as continued crystallization arrests further ascent). The equilibrium crystallization (+) sequence is: + amphibole, + plagioclase, + apatite,+ orthopyroxene, followed by breakdown (–) of amphibole and apatite, and finally silica saturation.

Closed-system degassing (Scenario B) Closed-system degassing of H_2O–CO_2-saturated magma differs substantially from the pure-H_2O case (Fig. 11b). Here the vapor saturation pressure of 300 MPa is determined by our initial melt composition (5.3 wt% H_2O and 1282 ppm CO_2, after Blundy et al. 2010), whereupon the magma contains 25 wt% plagioclase, orthopyroxene, and oxide crystals; equilibrium plagioclase is considerably more albitic than in the water-saturated system (An_{41} versus An_{53}). Amphibole only begins to crystallize on decompression to 200 MPa, by which pressure ~50% of the melt's original CO_2 has exsolved (from 1280 to 560 ppm). Significantly, negligible crystallization takes place over this pressure interval, and plagioclase compositions remain nearly constant, as does melt water content. Noticeable changes in phase proportions and compositions only occur at P <100 MPa (H_2O <4.3 wt%, CO_2 <60 ppm), where the closed-system degassing path parallels that of water-saturated ascent. The magma grazes the apatite stability field before amphibole

begins to breakdown (110 MPa), followed by apatite resorption (80 MPa) and silica saturation (25 MPa). Although the late crystallization sequence is identical to the water-saturated scenario (– amphibole, – apatite, + silica), the early crystallization sequence is distinct (plagioclase/orthopyroxene, + amphibole, + apatite).

Two key differences between the water-saturated and closed-system scenarios are (a) the sequence of crystallization, and (b) the pressure range over which crystallization occurs. In the first instance, the early appearance of amphibole indicates the presence of water-rich fluids at depth (XH_2O^{fl} >0.9). These distinctions may be more pronounced in less evolved compositions or at lower temperatures, where the amphibole stability field is larger (e.g., Rutherford et al. 1985; Rutherford and Devine 1988; Gardner et al. 1995b). Fig. 12 shows that closed-system degassing is ineffective at driving isothermal crystallization in the 300–100 MPa pressure interval, while 30% crystallization of the same magma occurs over this interval under water-saturated conditions. Although both of these magmas will eventually achieve high crystallinities (~60 wt% by 25 MPa), they will experience considerably different P–crystallinity paths en route (Fig. 11h), with implications for the depth evolution of magma properties (e.g., density, viscosity, and buoyancy).

Vapor-buffered ascent (Scenario C) Vapor-buffered ascent at XH_2O^{fl} = 0.8 follows a trajectory broadly similar to water-saturated decompression, in that crystallization proceeds continuously along the degassing path (Fig. 11c). Crystallization of both plagioclase and orthopyroxene begins at higher pressure than in the pure-water system (350 versus 220 MPa), and the melt contains 7 wt% crystals at the onset of decompression from 300 MPa. Because the melt is buffered to higher CO_2 contents at all pressures, crystallinity is always higher than during water-saturated ascent; this offset is greatest at high pressures. In contrast to closed-system degassing, H_2O and CO_2 decrease in tandem, yielding increasingly albitic plagioclase throughout the decompression interval. Anorthite contents decrease from An_{50} at 300 MPa, to An_{41} at 200 MPa, to An_{35} at 100 MPa. As above, amphibole follows plagioclase and orthopyroxene in the crystallization sequence and is stable over a relatively narrow range of pressures (220–130 MPa) compared to the water-saturated case. Vapor-buffered magma encounters silica saturation at higher pressures (45 MPa) than in the preceding examples. The crystallization sequence is the same as during closed-system degassing, except that apatite is not stable anywhere along this degassing path. This demonstrates an important feature of vapor-buffered ascent: the phase assemblage at any given pressure is sensitive to the composition of the buffering fluid. A magma buffered by more CO_2-rich vapor may only

graze the amphibole stability field (e.g., XH_2O^{fl} = 0.75), or may pass entirely outside of it (XH_2O^{fl} = 0.70). Fluid composition also determines the silica saturation pressure during isothermal equilibrium crystallization.

Isobaric vapor fluxing (Scenario D) Our final example considers fluxing of initially CO_2-free magma (XH_2O^{fl} ~1.0) by CO_2-rich vapor (XH_2O^{fl} ~0.6) at an arbitrary pressure of 200 MPa (Fig. 11d). Initially, the system is saturated with plagioclase + amphibole + apatite + Fe–Ti oxides; orthopyroxene begins to crystallize soon after the onset of fluxing, joining the assemblage where the isobar intersects the phase boundary ($XH_2O^{fl} \approx$ 0.95 mol%; Fig. 9). Continued fluxing leads to destabilization of amphibole ($XH_2O^{fl} \approx$ 0.70) and, eventually, to silica saturation ($XH_2O^{fl} \approx$ 0.60) at significantly higher pressure than in any of the scenarios described above. Both crystallinity and plagioclase composition evolve steadily as melt water content decreases. Although the magnitudes of these changes are subdued relative to preceding scenarios, they are significant: anorthite content decreases by 12 mol% (An_{49} to An_{37}) and total crystallinity increases three-fold (10 to 32 wt%) during fluxing from XH_2O^{fl} = 1.0 to 0.6. Importantly in this case all of the observed changes occur at constant temperature and pressure, and melt CO_2 content increases (while total dissolved volatile content decreases) during crystallization (Fig. 11e). The crystallization sequence is plagioclase/amphibole/apatite, – apatite, + orthopyroxene, – amphibole, + silica.

The intersection of phase boundaries and vapor isopleths gives rise to an interesting feature of our crystallization model: an apparent maximum in the capacity of vapor fluxing to drive crystallization of a melt (hereafter "fluxing efficiency"). This is illustrated in Fig. 12, which plots equilibrium crystallinity versus pressure, contoured for fluid composition; the offset between contours represents the amount of crystallization driven by re-equilibration with a vapor of specified composition. Offsets show maxima near 200 MPa that are a simple consequence of phase equilibria (Fig. 12 inset): at low pressures, isopleths are closely spaced relative to crystallinity contours, and a large change in vapor composition results in minimal crystallization. A similar effect is observed at higher pressures, but for different reasons; above the plagioclase liquidus, CO_2-rich vapor compositions are required to drive substantial crystallization of plagioclase ± orthopyroxene. This effect is exacerbated by the steepening of isobars with increasing pressure (e.g. Figs. 2 and 10; Papale et al. 2006).

Fig. 12 indicates that fluxing of a CO_2-bearing fluid, if it occurs, has a pressure or depth of maximum efficiency where a modest change in fluid composition is likely to impose a measurable petrologic signature (200–250 MPa for the Sugar Bowl rhyodacite). Interestingly,

this same pressure range corresponds to that of an inferred upper crustal storage region existing prior to and during the 1980–1986 eruptions of Mount St. Helens (220–320 MPa), as indicated by a combination of geophysical (Scandone and Malone, 1985; Lees 1992; Moran, 1994), petrologic (Blundy and Cashman, 2001; Cashman and McConnell, 2005; Blundy et al. 2008), and experimental (Rutherford et al. 1985; Rutherford and Devine 1988; Gardner et al. 1995b) constraints. The coincidence of inferred storage pressures with those of maximum fluxing efficiency suggests that vapor mobility may have played an important role in modulating the physical and chemical properties of magmas erupted during this period, perhaps encouraging magmas to stall by increasing their bulk viscosity. If gas fluxing was enhanced by the overburden release accompanying Plinian eruption (as suggested by an increase in deep seismicity and non-eruptive CO_2 emissions in the weeks and months following the May 18th climactic eruption; Weaver et al. 1981; Scandone and Malone 1985; Harris and Rose 1996), this phenomenon may ultimately have contributed to self-sealing of the chamber and the transition to effusive behavior.

4.3 Application to natural datasets

Our model illustrates how phase equilibria constraints can facilitate the integration of petrologic data to interpret isothermal magmatic processes (i.e. degassing) operating beneath arc volcanoes. Experiments identify several generic features of the Sugar Bowl rhyodacite system that are sensitive indicators of degassing path. These include the crystallization sequence, which differs in each of the examples discussed above, and, to a lesser extent, shifting proportions of mafic phases (e.g. opx), which may be recorded in melt inclusion and groundmass glass compositions. The latter may be diagnostic in systems with higher proportions of amphibole and/or orthopyroxene. A key observation arising from our illustrations, however, is that water concentrations alone provide limited information on processes of coupled degassing and crystallization, because isothermal phase equilibria are so strongly controlled by melt H_2O content (e.g., Fig. 10). For example, isothermal H_2O loss under polybaric (decompression) and isobaric (gas fluxing) conditions may yield indistinguishable relationships between H_2O concentrations and geochemical tracers of melt crystallinity (e.g., glass SiO_2 and K_2O contents; Blundy and Cashman 2005), though the processes driving crystallization in these cases are fundamentally different. From this perspective, melt CO_2 concentrations are considerably more useful. Figs. 11b–d show that crystallinity–CO_2 and An–CO_2 relationships are sensitive to vapor composition and

abundance and have potential as tracers of magmatic degassing. Although in practice it is difficult to match a melt inclusion of known CO_2 content to host plagioclase of known An content (Cashman and Blundy 2013), alternative indices of melt evolution, such as highly-incompatible trace elements (e.g., Rb, U), or trace elements with compositionally-dependent partition coefficients in plagioclase (e.g., Sr, Ba), could provide a more direct means of assessing these trends (e.g., Wallace et al. 1999; Roberge et al. 2013).

Our model may also guide interpretation of melt inclusion datasets where both CO_2 and H_2O concentrations are known. At equilibrium, for example, inclusion compositions should plot within the stability field of the erupted assemblage (Figs. 9a–b), as is the case for most melt inclusions from the May 18th, 1980, Plinian eruption (Blundy et al. 2010). This observation is consistent with the absence of amphibole breakdown rims in pyroclasts from these deposits (Rutherford and Hill 1993). It also provides corroborating evidence that Plinian magma ascended rapidly from high pressure, without time for significant re-equilibration. Many melt inclusions from post-May 18th eruptions plot within the silica stability field, in keeping with the presence of crystobalite and/or tridymite in the groundmass of samples from the 1980–1986 eruptions (Hoblitt and Harmon 1993; Blundy and Cashman 2001; Cashman and McConnell 2005; Pallister et al. 2008), for which the Sugar Bowl composition is a proxy. In contrast, originally water-rich inclusions in slowly ascending magmas, or magmas that stall following rapid ascent, may lose H_2O via diffusion through the host crystal walls (Portnyagin et al. 2008; Gaetani et al. 2012; Lloyd et al. 2013) or by continued communication with the melt during progressive degassing (Blundy and Cashman 2005; Humphreys et al. 2008). Such open-system behavior is suggested by inclusion compositions plotting below the solidus in Fig. 9b. Likewise, amphibole-hosted melt inclusions with vapor compositions plotting outside the amphibole stability field give compelling evidence of open-system behavior. Where volatile concentrations are suggestive of vapor fluxing (e.g., Rust et al. 2004; Johnson et al. 2008; Blundy et al. 2010), projections of the type in Fig. 9 can further constrain the nature of petrologic adjustments expected to accompany the inferred shift in fluid composition. These adjustments may be diagnostic; for example, a CO_2-rich, silica-saturated magma with textural evidence of amphibole breakdown would be indicative of high-pressure vapor fluxing (Fig. 9).

Degassing and crystallization are tandem processes in volcanic systems that together modulate the physico-chemical properties of magmas. Our experimental results provide a new framework for interpreting degassing behavior, as recorded in the compositions and textures of crystal-bearing volcanic rocks. We conclude that projecting phase equilibria into

CO_2–H_2O space is a useful tool for integrating experimental and natural datasets. Although the melt inclusion record is complex, our approach shows how phase equilibria constraints may be used to corroborate patterns in melt inclusion data, assess the extent of equilibrium (or disequilibrium) during degassing-driven crystallization, and identify petrologic features diagnostic of degassing style.

Acknowledgments

JMR was supported by a University of Bristol postgraduate scholarship; JDB by European Research Council Advanced Grant CRITMAG; ACR and MCSH by Royal Society URFs; and RB by Deutsche Forschungsgemeinschaft funding. We thank R. Brooker and K. Cashman for helpful discussions. We are also grateful for assistance on the University of Edinburgh ion microprobe from R. Hinton and C.J. der Hoog, and on the University of Bristol electron microprobes and SEM from B. Buse and S. Kearns.

References

Andersen D, Lindsley D (1988) Internally consistent solution models for Fe–Mg–Mn–Ti oxides: Fe–Ti oxides. Am Mineral 73:714–726.

Anderson G, Burnham C (1983) Feldspar solubility and the transport of aluminum under metamorphic conditions. Am J Sci 283:283–297

Annen C, Blundy J, Sparks R (2006) The genesis of intermediate and silicic magmas in deep crustal hot zones. J Petrology 47:505–539

Baker D, Alletti M (2012) Fluid saturation and volatile partitioning between melts and hydrous fluids in crustal magmatic systems: The contribution of experimental measurements and solubility models. Earth Sci R 114:298–324

Berlo K, Blundy J, Turner S, Hawkesworth C (2007) Textural and chemical variation in plagioclase phenocrysts from the 1980 eruptions of Mount St. Helens, USA. Contr Min P 154:291–308

Berndt J, Liebske C, Holtz F, Freise M, Nowak M, Ziegenbein D, Hurkuck W, Koepke J (2002) A combined rapid-quench and H_2-membrane setup for internally heated pressure vessels: Description and application for water solubility in basaltic melts. Am Mineral 87: 1717-1726.

Blank J, Stolper E, Carroll M (1993) Solubilities of carbon dioxide and water in rhyolitic melt at 850 °C and 750 bars. Earth Plan 119:27–36

Blundy J, Cashman K (2001) Ascent-driven crystallization of dacite magmas at Mount St. Helens, 1980–1986. Contr Min P 140:631–650

Blundy J, Cashman K (2005) Rapid decompression-driven crystallization recorded by melt inclusions from Mount St. Helens volcano. Geology 33:793–796

Blundy J, Cashman K (2008) Petrologic reconstruction of magmatic system variables and processes. In: Putirka K, Tepley F (eds) Minerals, inclusions, and volcanic processes, Rev Min Geo, pp 179–239

Blundy J, Cashman K, Humphreys M (2006) Magma heating by decompression-driven crystallization beneath andesite volcanoes. Nature 443:76–80

Blundy J, Cashman K, Berlo K (2008) Evolving magma storage conditions beneath Mount St. Helens inferred from chemical variations in melt inclusions from the 1980–1986 and current (2004–2006) eruptions. In: Sherrod D, Scott W, Stauffer P (eds) A volcano rekindled: The renewed eruption of Mount St. Helens, 2004–2006, USGS Prof Pap 1750, pp 755– 790

Blundy J, Cashman K, Rust A, Witham F (2010) A case for CO_2-rich arc magmas. Earth Plan 290:289–301

Botcharnikov R, Almeev R, Koepke J, Holtz F (2008) Phase relations and liquid lines of descent in hydrous ferrobasalt – implications for the Skaergaard intrusion and Columbia River flood basalts. J Petrology 49:1687–1727

Brugger C, Hammer J (2010) Crystallization kinetics in continuous decompression experiments: Implications for interpreting natural magma ascent processes. J Petrology 51:1941–1965

Burgisser A, Scaillet B (2007) Redox evolution of a degassing magma rising to the surface. Nature 445:194–197

Burnham C, Jahns R (1962) A method for determining the solubility of water in silicate melts. Am J Sci 260:721–745

Carmichael I (2002) The andesite aqueduct: Perspectives on the evolution of intermediate magmatism in west-central (105–99 W) Mexico. Contr Min P 143:641–663

Carmichael I, Nicholls J (1967) Iron-titanium oxides and oxygen fugacities in volcanic rocks. J Geo R 72:4665–4687

Cashman K (1992) Groundmass crystallization of Mount St. Helens dacite, 1980–1986: A tool for interpreting shallow magmatic processes. Contr Min P 109:431–449

Cashman K (1993) Relationship between plagioclase crystallization and cooling rate in basaltic melts. Contr Min P 113:126–142

Cashman K, Blundy J (2013) Petrological cannibalism: The chemical and textural consequences of incremental magma body growth. Contr Min P 166:703–729

Cashman K, McConnell S (2005) Multiple levels of magma storage during the 1980 summer eruptions of Mount St. Helens, WA. B Volcanol 68:57–75

Castro J, Dingwell D (2009) Rapid ascent of rhyolitic magma at Chaiten volcano, Chile. Nature 461:780–784

Cichy S, Botcharnikov R, Holtz F, Behrens H (2011) Vesiculation and microlite crystallization induced by decompression: A case study of the 1991–1995 Mt. Unzen eruption (Japan). J Petrology 52:1469–1492

Cooper K, Reid M (2003) Re-examination of crystal ages in recent Mount St. Helens lavas: Implications for magma reservoir processes. Earth Plan 213:149–167

Couch S, Sparks R, Carroll M (2003) The kinetics of degassing-induced crystallization at Soufriere Hills Volcano, Montserrat. J Petrology 44:1477–1502

Devine J, Gardner J, Brack H, Layne G, Rutherford M (1995) Comparison of microanalytical methods for estimating H_2O contents of silicic volcanic glasses. Am Mineral 80:319–328

Di Carlo I, Pichavant M, Rotolo S, Scaillet B (2006) Experimental crystallization of a high-K arc basalt: the golden pumice, Stromboli volcano (Italy). J Petrology 47:1317–1343

Dixon J, Stolper E, Holloway J (1995) An experimental study of water and carbon dioxide solubilities in mid ocean ridge basaltic liquids 1. Calibration and solubility models. J Petrology 36:1607–1631

Duan Z, Zhang Z (2006) Equation of state of the H_2O, CO_2, and H_2O–CO_2 systems up to 10 GPa and 2573.15 K: Molecular dynamics simulations with ab initio potential surface. Geoch Cos A 70:2311– 2324

Ebadi A, Johannes W (1991) Beginning of melting and composition of first melts in the system Qz–Ab–Or–H_2O–CO_2 . Contr Min P 106:286–295

Eggler D, Burnham C (1973) Crystallization and fractionation trends in the system andesite-H_2O -CO_2 -O2 at pressures to 10 kb. Geol S Am B 84:2517–2532

Feig S, Koepke J, Snow J (2006) Effect of water on tholeiitic basalt phase equilibria: an experimental study under oxidizing conditions. Contr Min P 152:611–638

Frost BR (1991) Introduction to oxygen fugacity and its petrologic importance. Rev Min Geo 25(1):1–9

Gaetani G, O'Leary J, Shimizu N, Bucholz C, Newville M (2012) Rapid reequilibration of H_2O and oxygen fugacity in olivine-hosted melt inclusions. Geology 40:915–918

Gardner J, Carey S, Rutherford M, Sigurdsson H (1995a) Petrologic diversity in Mount St. Helens dacites during the last 4,000 years – Implications for magma mixing. Contr Min P 119:224–238

Gardner J, Rutherford M, Carey S, Sigurdsson H (1995b) Experimental constraints on pre-eruptive water contents and changing magma storage prior to explosive eruptions of Mount St. Helens volcano. B Volcanol 57:1–17

Geschwind C, Rutherford M (1992) Cummingtonite and the evolution of the Mount St. Helens (Washington) magma system: An experimental study. Geology 20:1011–1014

Ghiorso M, Evans B (2008) Thermodynamics of rhombohedral oxide solid solutions and a revision of the Fe−Ti two oxide geothermometer and oxygen-barometer. Am J Sci 308:957–1039

Gonnermann H, Manga M (2005) Nonequilibrium magma degassing: Results from modeling of the ca. 1340 AD eruption of Mono Craters, California. Earth Plan 238:1–16

Halliday A, Fallick A, Dickin A, Mackenzie A, Stephens W, Hildreth W (1983) The isotopic and chemical evolution of Mount St. Helens. Earth Plan 63:241–256

Hammer J (2008) Experimental studies of the kinetics and energetics of magma crystallization. In: Putirka K, Tepley F (eds) Minerals, inclusions, and volcanic processes, Rev Min Geo, pp 9–59

Hammer J, Rutherford M (2002) An experimental study of the kinetics of decompression-induced crystallization in silicic melt. J Geo R 107:1–23

Hammer J, Rutherford M (2003) Petrologic indicators of preeruption magma dynamics. Geology 31:79–82

Hammer J, Rutherford M, Hildreth W (2002) Magma storage prior to the 1912 eruption at Novarupta, Alaska. Contr Min P 144:144–162

Harris D, Rose W (1996) Dynamics of carbon dioxide emissions, crystallization, and magma ascent: Hypotheses, theory, and applications to volcano monitoring at Mount St. Helens. B Volcanol, 58:163–174

Hauri E, Wang J, Dixon J, King P, Mandeville C, Newman S (2002) SIMS analysis of volatiles in silicate glasses 1. Calibration, matrix effects, and comparisons with FTIR. Chem Geol 183:99–114

Heliker C (1995) Inclusions in Mount St. Helens dacite erupted from 1980 through 1983. J Volcanol 66:115–135

Hoblitt R, Harmon R (1993) Bimodal density distribution of cryptodome dacite from the 1980 eruption of Mount St. Helens, Washington. B Volcanol 55:421– 437

Holtz F, Pichavant M, Barbey P, Johannes W (1992) Effects of H_2O on liquidus phase relations in the haplogranite system at 2 and 5 kbar. Am Mineral 77:1223– 1241

Holtz F, Sato H, Lewis J, Behrens H, Nakada S (2005) Experimental petrology of the 1991–1995 Unzen dacite, Japan. Part I: Phase relations, phase composition and pre-eruptive conditions. J Petrology 46:319–337

Ihinger P, Hervig R, Mcmillan P (1994) Analytical methods for volatiles in glasses. In: Carroll M, Holloway J (eds) Volatiles in magmas, Rev Min, pp 67–121

Johnson E, Wallace P, Cashman K, Granados H, Kent AJ (2008) Magmatic volatile contents and degassing-induced crystallization at Volcán Jorullo, Mexico: Implications for melt evolution and the plumbing systems of monogenetic volcanoes. Earth Plan 269:478–487

Kennedy G, Wasserburg G, Heard H, Newton R (1962) The upper three-phase region in the system SiO_2–H_2O. Am J Sci 260:501–521

Kress V, Carmichael I (1991) The compressibility of silicate liquids containing Fe_2O_3 and the effect of composition, temperature, oxygen fugacity and pressure on their redox states. Contr Min P 108:82–92

Lees J (1992) The magma system of Mount St. Helens: Non-linear high-resolution P-wave tomography. J Volcanol 53:103–116

Lepage L (2003) ILMAT: An Excel worksheet for ilmenite–magnetite geothermometry and geobarometry. Comput Geos 29:673–678

Lesne P, Kohn S, Blundy J, Witham F, Botcharnikov R, Behrens H (2011) Experimental simulation of closed-system degassing in the system basalt–H_2O–CO_2–S–Cl. J Petrology 52:1737–1762

Liu Y, Zhang Y, Behrens H (2005) Solubility of H_2O in rhyolitic melts at low pressures and a new empirical model for mixed H_2O–CO_2 solubility in rhyolitic melts. J Volcanol 143:219–235

Lloyd A, Plank T, Ruprecht P, Hauri E, Rose W (2013) Volatile loss from melt inclusions in pyroclasts of differing sizes. Contr Min P 165:129–153

Mangan M, Sisson T (2000) Delayed, disequilibrium degassing in rhyolite magma: Decompression experiments and implications for explosive volcanism. Earth Plan 183:441–455

Martel C (2012) Eruption dynamics inferred from microlite crystallization experiments: Application to plinian and dome-forming eruptions of Mt. Pelee (Martinique, Lesser Antilles). J Petrology 53:699–725

Martel C, Schmidt B (2003) Decompression experiments as an insight into ascent rates of silicic magmas. Contr Min P 144:397–415

Matthews W, Linnen R, Guo Q (2003) A filler-rod technique for controlling redox conditions in cold-seal pressure vessels. Am Mineral 88:701–707

Merzbacher C, Eggler D (1984) A magmatic geohygrometer: Application to Mount St. Helens and other dacitic magmas. Geology 12:587–590

Moore G (2008) Interpreting H_2O and CO_2 contents in melt inclusions: Constraints from solubility experiments and modeling. In: Putirka K, Tepley F (eds) Minerals, inclusions, and volcanic processes, Rev Min Geo, pp 333–361

Moran S (1994) Seismicity at Mount St. Helens, 1987– 1992: Evidence for repressurization of an active magmatic system. J Geo R 99:4341– 4354

Mullineaux D (1986) Summary of pre-1980 tephra-fall deposits erupted from Mount St. Helens, Washington State, USA. B Volcanol 48:17–26

Newman S, Lowenstern J (2002) VolatileCalc: A silicate melt–H_2O–CO_2 solution model written in Visual Basic for Excel. Comput Geos 28:597–604

O'Neill H, Pownceby M (1993) Thermodynamic data from redox reactions at high temperatures. I. An experimental and theoretical assessment of the electrochemical method using stabilized zirconia electrolytes, with revised values for the Fe–"FeO", Co−CoO, Ni−NiO and Cu−Cu_2O oxygen buffers, and new data for the W−WO_2 buffer. Contr Min P 114(3):296–314

Pallister J, Hoblitt D Rand Crandell, Mullineaux D (1992) Mount St. Helens a decade after the 1980 eruptions: Magmatic models, chemical cycles, and a revised hazards assessment. B Volcanol 54:126–146

Pallister J, Thornber C, Cashman K, Clynne M, Lowers H, Mandeville C, Brownfield I, Meeker G (2008) Petrology of the 2004–2006 Mount St. Helens lava dome – Implications for magmatic plumbing and eruption triggering. In: Sherrod D, Scott W, Stauffer P (eds) A volcano rekindled: The renewed eruption of Mount St. Helens, 2004–2006, USGS Prof Pap 1750, pp 647–702

Papale P (2005) Determination of total H_2O and CO_2 budgets in evolving magmas from melt

inclusion data. J Geo R 110:1–13

Papale P, Moretti R, Barbato D (2006) The compositional dependence of the saturation surface of H_2O+CO_2 fluids in silicate melts. Chem Geol 229:78–95

Pichavant M, Martel C, Bourdier J, Scaillet B (2002) Physical conditions, structure, and dynamics of a zoned magma chamber: Mount Pelee (Martinique, Lesser Antilles Arc). J Geo R 107:1–29

Pichavant M, Costa F, Burgisser A, Scaillet B, Martel C, Poussineau S (2007) Equilibration scales in silicic to intermediate magmas – Implications for experimental studies. J Petrology 48:1955–1972

Pichavant M, Di Carlo I, Le Gac Y, Rotolo SG, Scaillet B (2009) Experimental constraints on the deep magma feeding system at Stromboli volcano, Italy. J Petrology 50:601–624

Portnyagin M, Almeev R, Matveev S, Holtz F (2008) Experimental evidence for rapid water exchange between melt inclusions in olivine and host magma. Earth Plan 272:541–552

Putirka K (2008) Thermometers and barometers for volcanic systems. In: Putirka K, Tepley F (eds) Minerals, inclusions, and volcanic processes, Rev Min Geo, pp 61–120

Ridolfi F, Renzulli A (2012) Calcic amphiboles in calcalkaline and alkaline magmas: Thermobarometric and chemometric empirical equations valid up to 1,130 °C and 2.2 GPa. Contr Min P 163:877–895

Rust A, Cashman K, Wallace P (2004) Magma degassing buffered by vapor flow through brecciated conduit margins. Geology 32:349–352

Rutherford M, Devine J (1988) The May 18, 1980, eruption of Mount St. Helens 3. Stability and chemistry of amphibole in the magma chamber. J Geo R 93:11,949–11,959

Rutherford M, Devine J (2008) Magmatic conditions and processes in the storage zone of the 2004–2006 Mount St. Helens dacite. In: Sherrod D, Scott W, Stauffer P (eds) A volcano

rekindled: The renewed eruption of Mount St. Helens, 2004–2006, USGS Prof Pap 1750, pp 703–725

Rutherford M, Hill P (1993) Magma ascent rates from amphibole breakdown – An experimental study applied to the 1980-1986 Mount St. Helens eruptions. J Geo R 98:19,667–19,685

Rutherford M, Sigurdsson H, Carey S, Davis A (1985) The May 18, 1980, eruption of Mount St. Helens 1. Melt composition and experimental phase equilibria. J Geo R 90:2929–2947

Saunders K, Blundy J, Dohmen R, Cashman K (2012) Linking petrology and seismology at an active volcano. Science 336:1023–1027

Scaillet B, Evans B (1999) The 15 June 1991 eruption of Mount Pinatubo I. Phase equilibria and pre-eruption P– T–fO_2–fH_2O conditions of the dacite magma. J Petrology 40:381–411

Scaillet B, Pichavant M, Cioni R (2008) Upward migration of Vesuvius magma chamber over the past 20,000 years. Nature 455:216–239

Scandone R, Malone S (1985) Magma supply, magma discharge and readjustment of the feeding system of Mount St. Helens during 1980. J Volcanol 23:239–262

Scheidegger K, Federman A, Tallman A (1982) Compositional heterogeneity of tephras from the 1980 eruptions of Mount St. Helens. J Geo R 87:861–881

Shea T, Hammer J (2013) Kinetics of cooling and decompression-induced crystallization in hydrous mafic-intermediate magmas. J Volcanol 260:127–145

Sisson T, Ratajeski K, Hankins W, Glazner A (2005) Voluminous granitic magmas from common basaltic sources. Contr Min P 148:635–661

Smith D (1984) The Petrology and Geochemistry of High Cascade Volcanics in Southern Washington: Mount St. Helens Volcano and the Indian Heaven Basalt Field. Dissertation, Rice University

Smith D, Leeman W (1987) Petrogenesis of Mount St. Helens dacitic magmas. J Geo R 92:10,313–10,334

Stamper C, Melekhova E, Blundy J, Arculus R, Humphreys M, Brooker R (2014) Oxidised phase relations of a primitive basalt from Grenada, Lesser Antilles. Contr Min P 167:1–20

Stormer J (1983) The effects of recalculation on estimates of temperature and oxygen fugacity from analyses of multicomponent iron-titanium oxides. Am Mineral 68:586–594

Streck M, Broderick C, Thornber C, Clynne M, Pallister J (2008) Plagioclase populations and zoning in dacite of the 2004–2005 Mount St. Helens eruption: Constraints for magma origin and dynamics. In: Sherrod D, Scott W, Stauffer P (eds) A volcano rekindled: The renewed eruption of Mount St. Helens, 2004–2006, USGS Prof Pap 1750, pp 791–808

Tamic N, Behrens H, Holtz F (2001) The solubility of H_2O and CO_2 in rhyolitic melts in equilibrium with a mixed CO_2–H_2O fluid phase. Chem Geol 174:333–347

Tuttle O, Bowen N (1958) Origin of granite in the light of experimental studies in the system $NaAlSi_3O_8$–$KAlSi_3O_8$–SiO_2–H_2O. Geological Society of America

Weaver C, Grant W, Malone S, Endo E (1981) Post-May 18 seismicity: Volcanic and tectonic implications. USGS Prof Pap 1250:109–121

Figure Captions

Fig. 1 Representative back-scattered electron (BSE) images of experimental run products. (a) Experiment PSB26 (175 MPa, $XH_2O^{fl} = 0.99$), containing a typical phase assemblage of melt, vesicles (vesc), plagioclase (plag), amphibole (amph), and Fe-Ti oxides (ox). (b) Plagioclase, orthopyroxene, and Fe-Ti oxides in sample PSB33 (50 MPa, $XH_2O^{fl} = 0.92$). Note the change in plagioclase size and habit relative to (a), reflecting the lower melt water content of this run. (c) Coexisting cubic (magn) and rhombohedral (ilm) oxides in sample PSB50 (200 MPa, $XH_2O^{fl} = 0.81$). Although scarce, rhombohedral oxides can be readily identified by their tabular habits.

Fig. 2 Concentrations of dissolved H_2O and CO_2 in experimental glasses. (a) H_2O versus total pressure in runs saturated with pure H_2O. (b) CO_2 versus total pressure in runs saturated with a mixed H_2O–CO_2 vapor. Spread of CO_2 contents at constant pressure reflects variable fluid compositions. The solubilities of both species are strongly pressure-dependent. (c) CO_2 versus H_2O for runs at different P_{total}, illustrating the interdependence of H_2O and CO_2 solubilities. For clarity, data at intermediate pressure steps (225 and 175 MPa) are not shown. Solid lines are equilibrium isobars and dashed lines are isopleths of equilibrium vapor composition (labeled as mol% H_2O), both calculated after Papale et al. (2006).

Fig. 3 Comparison of experimental run pressures with vapor saturation pressures calculated from measured glass H_2O and CO_2 contents. Solubility models used in calculations are (a) Papale et al. (2006) and (b) VolatileCalc (Newman and Lowenstern, 2002). Grey lines are 1:1 lines. Dashed line in (a) is a linear fit to the experimental data, used to correct modeled pressures as detailed in the Discussion.

Fig. 4 Experimentally-determined pressure–fluid composition phase diagram for Sugar Bowl rhyodacite at 885 °C. Each grid represents a single run. Solid lines are phase boundaries, with phases labeled on the stable side of the boundary. Dashed lines contour measured melt water contents. Stars indicate two samples in which a phase inferred to be stable (based on phase equilibria of adjacent samples) was not observed by SEM (Table 2). In these cases, phase boundaries have been drawn consistent with run products that contain the phase of interest, due to the possibility that rare phases were either not intersected or inadvertently missed

during BSE observation. The quartz–albite–orthoclase–H_2O–CO_2 solidus at 885 °C is after Ebadi and Johannes (1991). Average uncertainty in XH_2O^{fl} is ±0.02, and uncertainties in run pressures are smaller than symbols.

Fig. 5 Total crystallinity of run products versus (a) P_{total} in water-saturated experiments ($XH_2O^{fl} \approx 1$) and (b) fluid composition in experiments at constant P_{total} (200 MPa). Crystallinity increases with both decreasing pressure and decreasing XH_2O^{fl} at constant temperature as a result of degassing. Errors in mass balance regressions (95% confidence intervals) and run pressures are typically smaller than symbols. Crystallinities have been calculated by mass balance except where noted in the supplementary materials.

Fig. 6 Select major element variation diagrams for experimental glasses (open circles). Red circles give the starting composition (DS-63; Table 1). All data are normalized to 100 wt% on an anhydrous basis. Error bars on experimental glasses give the 1σ variation of multiple spot analyses. Also shown are compositions of melt inclusion and matrix glasses erupted at Mount St. Helens since 1980 (light grey dots) and whole rock compositions dating predominantly from the Holocene (dark grey dots), taken from a suite of 535 published analyses (see Blundy et al. 2008 and references therein).

Fig. 7 Compositions of experimental plagioclases. (a) Endmember plagioclase compositions plotted on the Ab–An–Or feldspar ternary (white circles). Numbers at base indicate mol% An. Published plagioclase compositions for Mount St. Helens dacites are shown for reference (grey dots; Smith 1984; Cashman 1992; Gardner et al. 1995a; Cooper and Reid 2003; Streck et al. 2008; grey bar below ternary shows range of compositions reported as binary An–Ab, which could not be plotted individually; Scheidegger et al. 1982; Berlo et al. 2007). These include data from the 2004–2008, 1980–1986, Goat Rocks, Kalama, Pine Creek, and Smith Creek eruptive periods**.** Experimental compositions overlap with those in natural Sugar Bowl dacites (black dots and black bar; Smith 1984; Smith and Leeman 1987; Berlo et al. 2007). Plotted, but unreported, Sugar Bowl plagioclase compositions from Smith (1984) and Smith and Leeman (1987) have been visually estimated to the nearest mol% An and included in the black bar. (b) Anorthite content of plagioclase in water-saturated experiments ($XH_2O^{fl} \approx 1$) versus P_{total} and (c) anorthite content of plagioclase in experiments at P_{total} = 200 MPa versus fluid composition. Grey lines in (b) and (c) are linear fits to the experimental data with the coefficients provided.

Fig. 8 Compositions of experimental orthopyroxenes. (a) Experimental orthopyroxene compositions plotted on the En–Fs–Wo ternary. Numbers at base indicate mol% En. Published orthopyroxene compositions for Mount St. Helens dacites (grey dots) are shown for reference; data are predominantly from the 1980–1986 eruptions (Saunders et al. 2012) but include analyses from the Goat Rocks, Kalama, Pine Creek, and Swift Creek eruptive periods (Smith 1984; Smith and Leeman 1987). Plotted, but unreported, compositions from Smith and Leeman (1987) have been visually estimated to the nearest mol%. Also shown are orthopyroxene compositions for the Sugar Bowl rhyodacite (black dots; Smith 1984). Experimental orthopyroxene compositions overlap with those of Sugar Bowl and other dacites, but extend to higher En. (b) Orthopyroxene compositions versus fO_2, in log units relative to the NNO buffer. The enstatite content of experimental pyroxenes is broadly correlated with measured oxygen fugacities.

Fig. 9 (a) Endmember degassing paths (black arrows) and experimentally-determined, vapor-saturated phase equilibria projected in CO_2–H_2O space. Isobars (grey lines) and vapor isopleths (dashed grey lines, labeled as mol% H_2O) were modeled for the experimental starting composition after Papale et al. (2006); modeled saturation pressures have been corrected using the relationship in Fig. 3a. Paths depict a range of possible degassing scenarios: (A) water-saturated ascent; (B) closed-system degassing of a melt containing 5.3 wt% H_2O and 1282 ppm CO_2 (after Blundy et al. 2010); (C) vapor-buffered ascent at XH_2O^{fl} = 0.8; and (D) isobaric vapor fluxing at 200 MPa. In each example, water exsolution proceeds in the direction of the arrow. The initial composition of each path, as considered in the text, is shown with a solid circle, excepting Path B, which begins off the diagram. The y-axis is offset for clarity. (b) Melt inclusion compositions from the 1980–1986 eruptions of Mount St. Helens (Blundy et al. 2010; Cashman and Blundy 2013) overlain on projected phase equilibria of the Sugar Bowl rhyodacite. Symbols designate inclusions from the May 18th, 1980 Plinian eruption (dark blue circles), post-May 18th explosive eruptions (open squares), and post-May 18th effusive dome eruptions (light blue triangles).

Fig. 10 Examples of experimental data (closed symbols) and regression fits (red lines) used to parameterize phase abundances and compositions as a function of melt H_2O content. Open symbols show data excluded from regressions. All data were fitted with unweighted hyperbolic functions of the form $y = a + b[\tanh(cx + d)]$ or $y = a + b[\sinh(cx + d)]$. Examples

shown are (a) total crystallinity versus dissolved H_2O, (b) plagioclase anorthite content versus total crystallinity, (c) melt SiO_2 content versus dissolved H_2O, and (d) orthopyroxene abundance versus dissolved H_2O. The compositions of long-duration decompression experiments with equilibrium crystallinities (Riker et al. in review) have been used to anchor regressions at low water content. In order to extend parameterizations from the liquidus to the solidus, hyperbolic fits are constrained, where reasonable, by inferred solidus conditions (cf. Fig. 4). Error bars give the 1σ variation of multiple spot analyses, or, for phase abundances, the 95% confidence interval of the mass balance coefficient. Similar regressions have been obtained for plagioclase and oxide abundances. See text for regression equations.

Fig. 11 (a–d) Variations of phase proportions, plagioclase anorthite contents, and dissolved volatile concentrations in the Sugar Bowl rhyodacite along the modeled degassing paths shown in Fig. 9. Abundances are given for melt (white), plagioclase (light blue), orthopyroxene (light orange), amphibole (dark blue), and total oxides (dark orange). The crystallization sequence along each path is also shown. (e–h) Modeled variations in melt composition, plagioclase composition, and crystallinity as a function of total pressure. Degassing proceeds in the direction of the arrow.

Fig. 12 Modeled crystallinity of the Sugar Bowl rhyodacite as a function of pressure for fluids with XH_2O 0.6–1.0. Inset shows "efficiency" of vapor fluxing in driving crystallization of magma initially in equilibrium with a pure-water vapor (x-axis gives the difference between the modeled equilibrium crystallinity at the fluid composition of interest and that at $XH_2O^{fl} = 1$). Grey shaded area is the inferred pressure range of pre-eruptive magma storage prior to the 1980 eruption of Mount St. Helens (e.g. Rutherford et al. 1985; Scandone and Malone 1985; Rutherford and Devine 1988; Lees 1992; Moran 1994; Gardner et al. 1995b; Blundy and Cashman 2001; Blundy et al. 2008).

Figure1
Click here to download Figure: fig2.tif

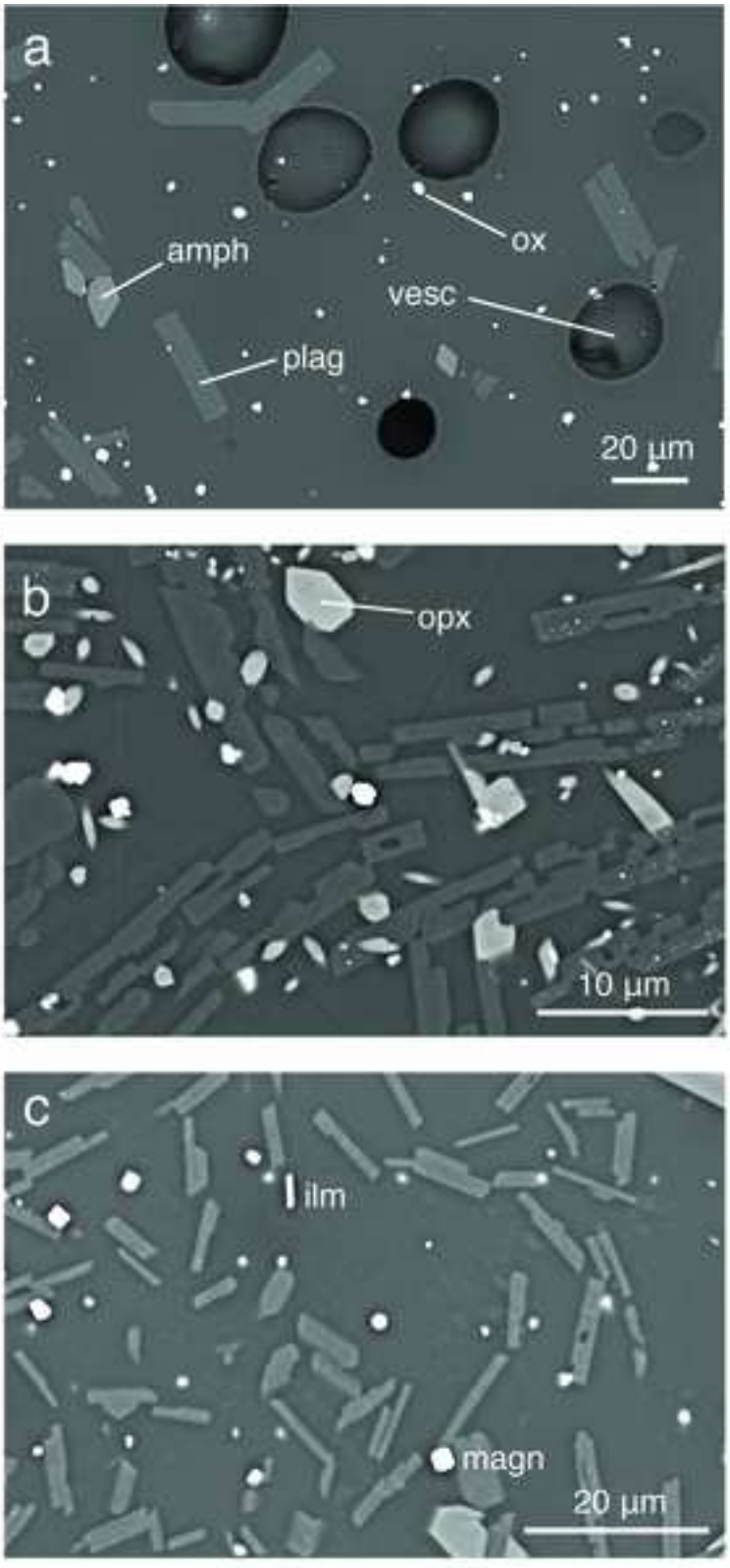

Figure2
Click here to download Figure: fig4.eps

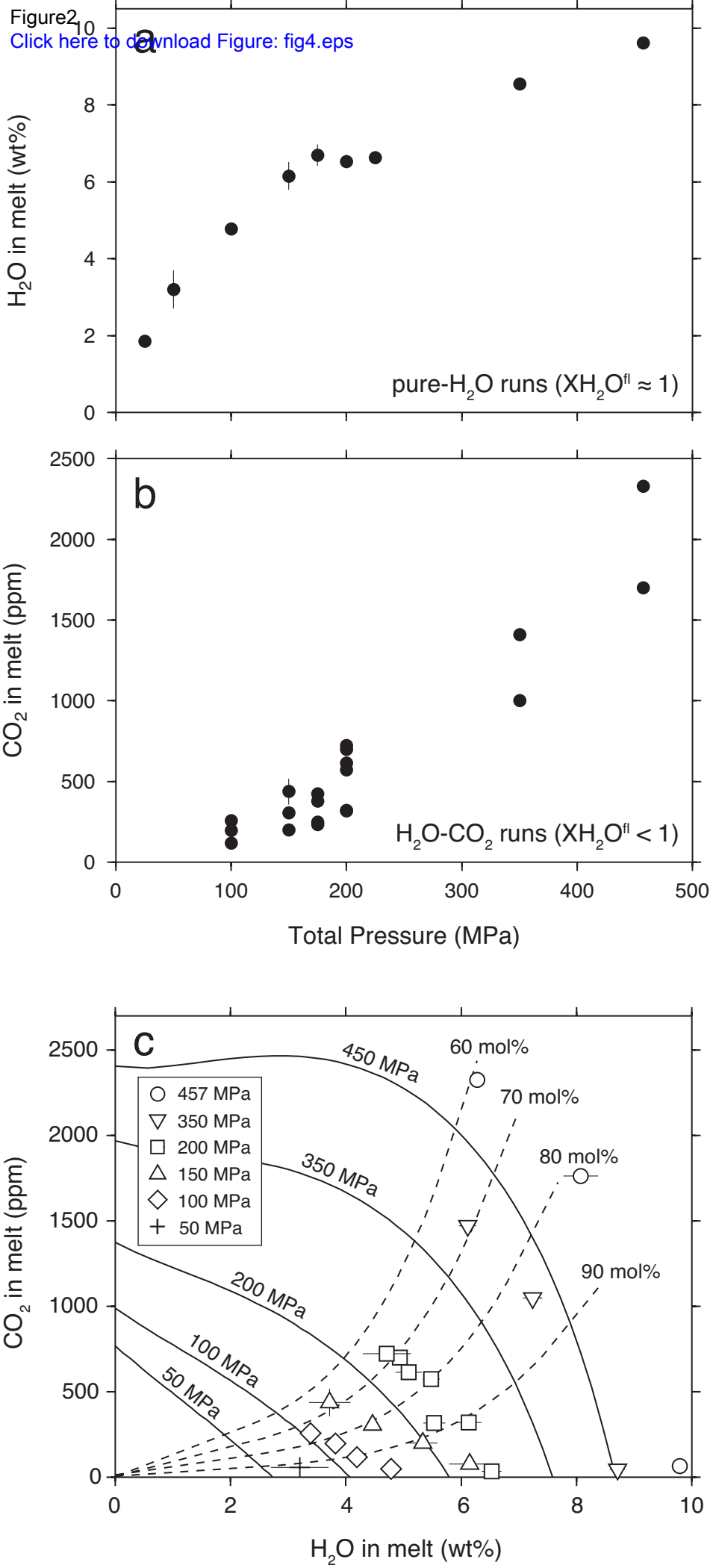

Figure3
Click here to download Figure: fig5.eps

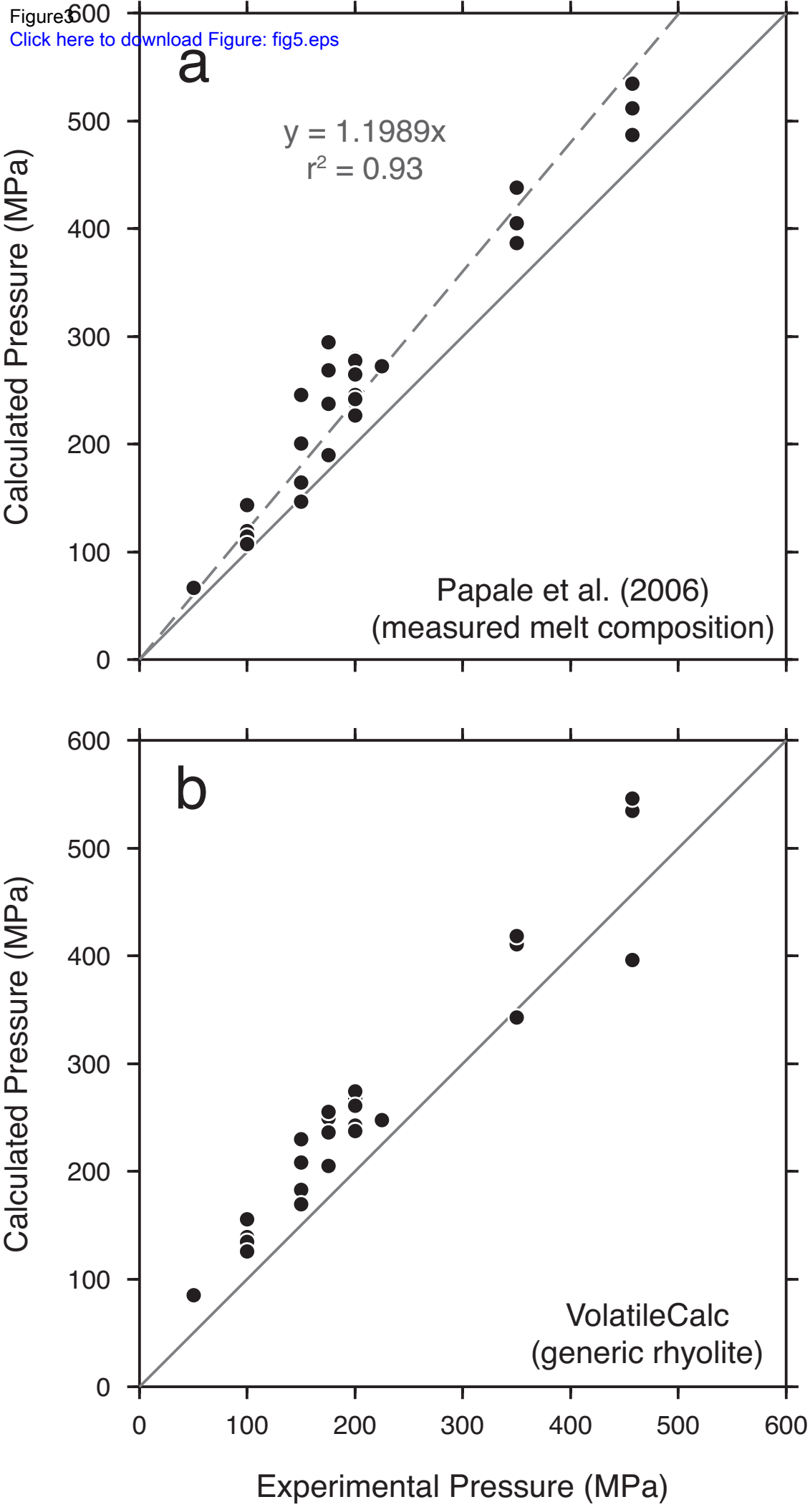

Figure4
Click here to download Figure: fig6.eps

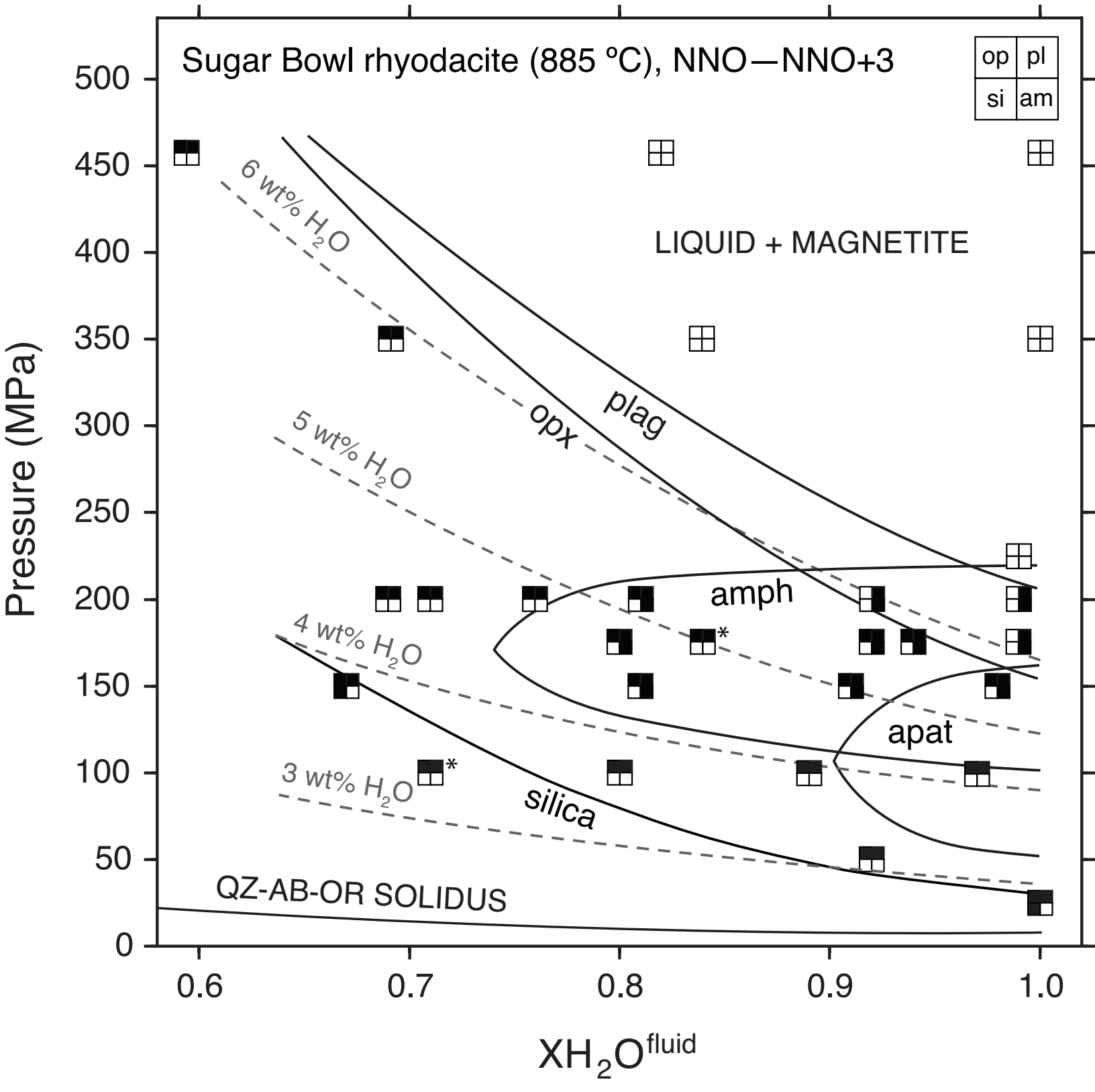

Figure 5
Click here to download Figure: fig7.eps

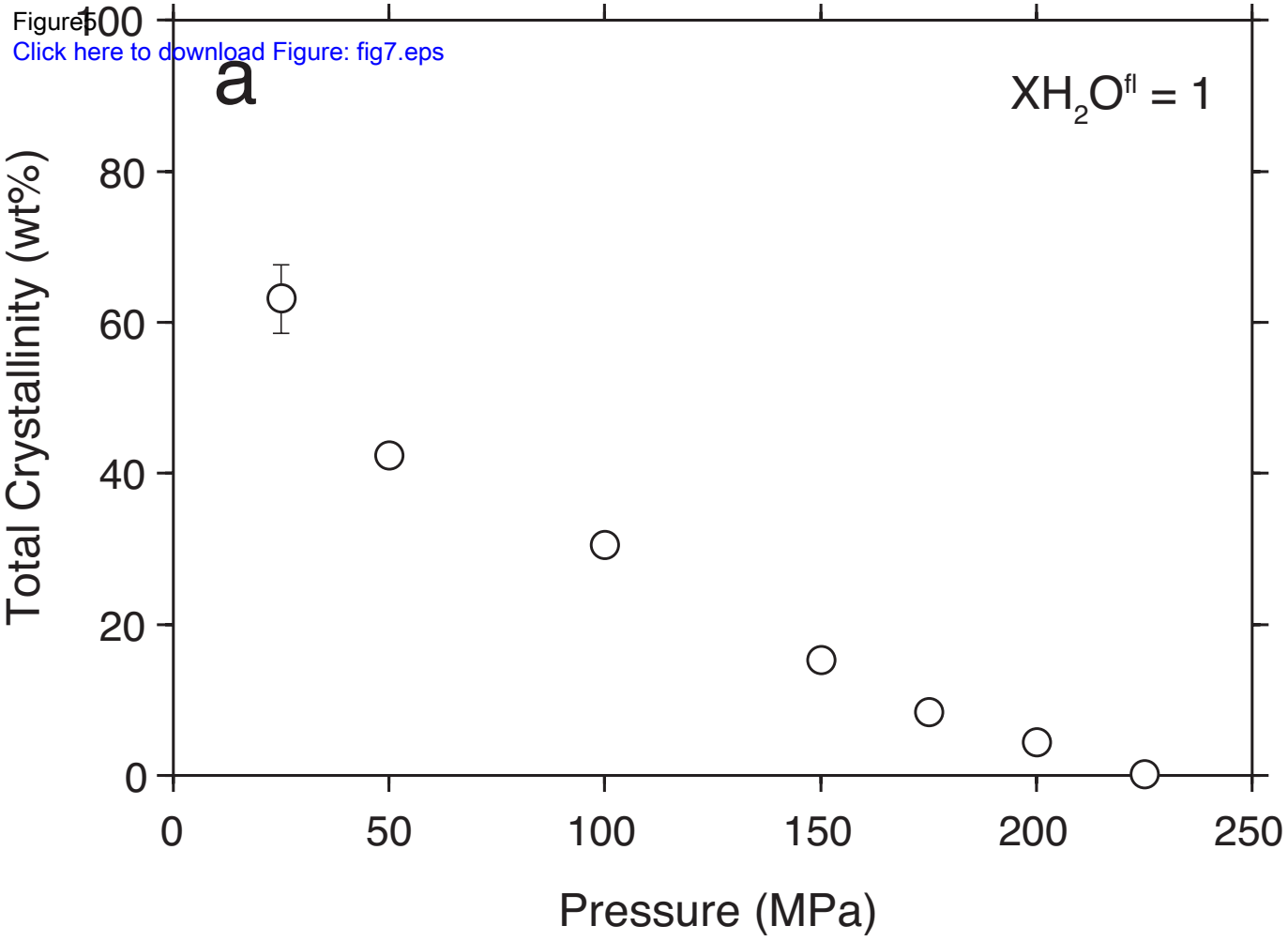

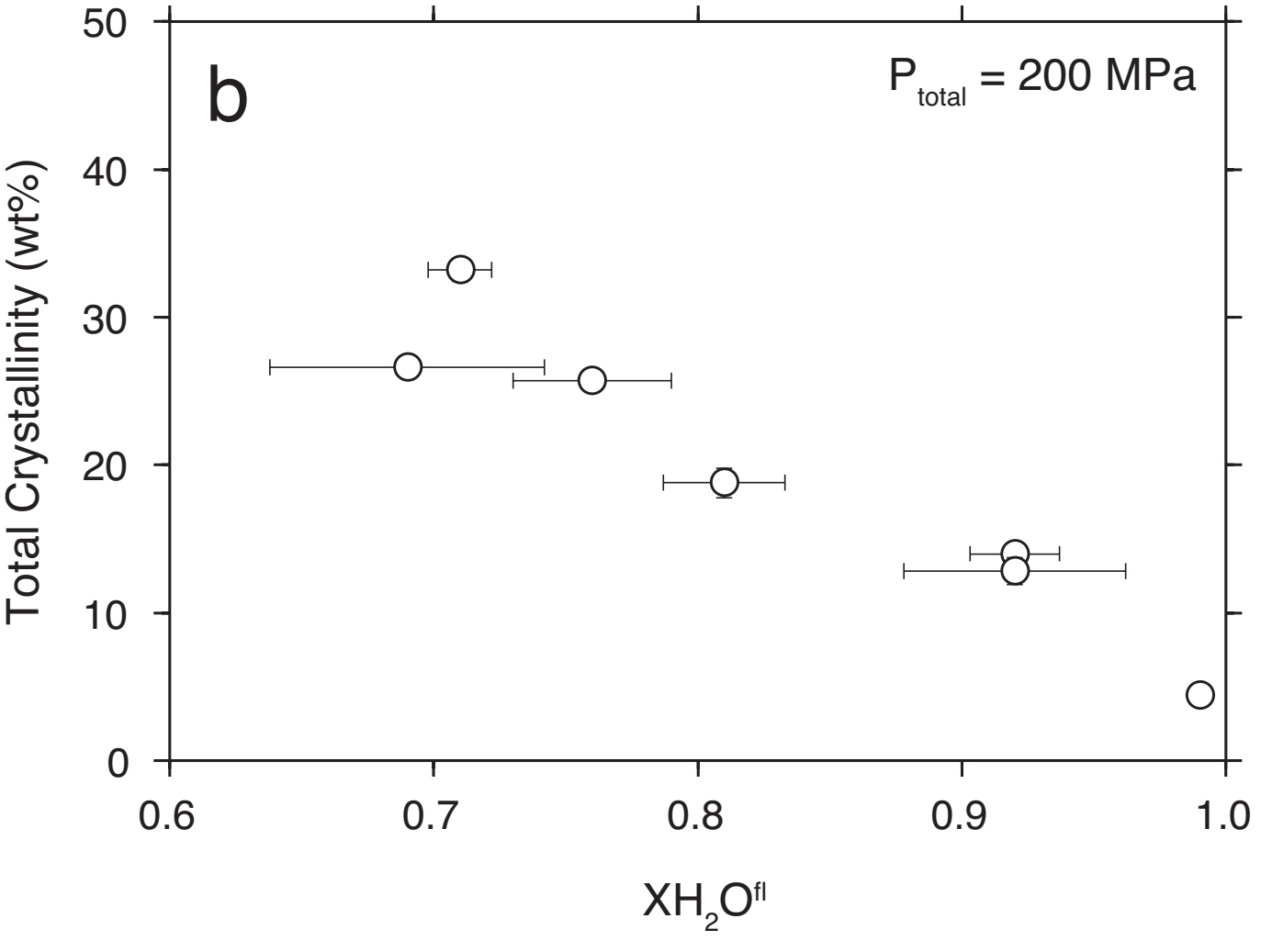

Figure8
Click here to download Figure: fig8.eps

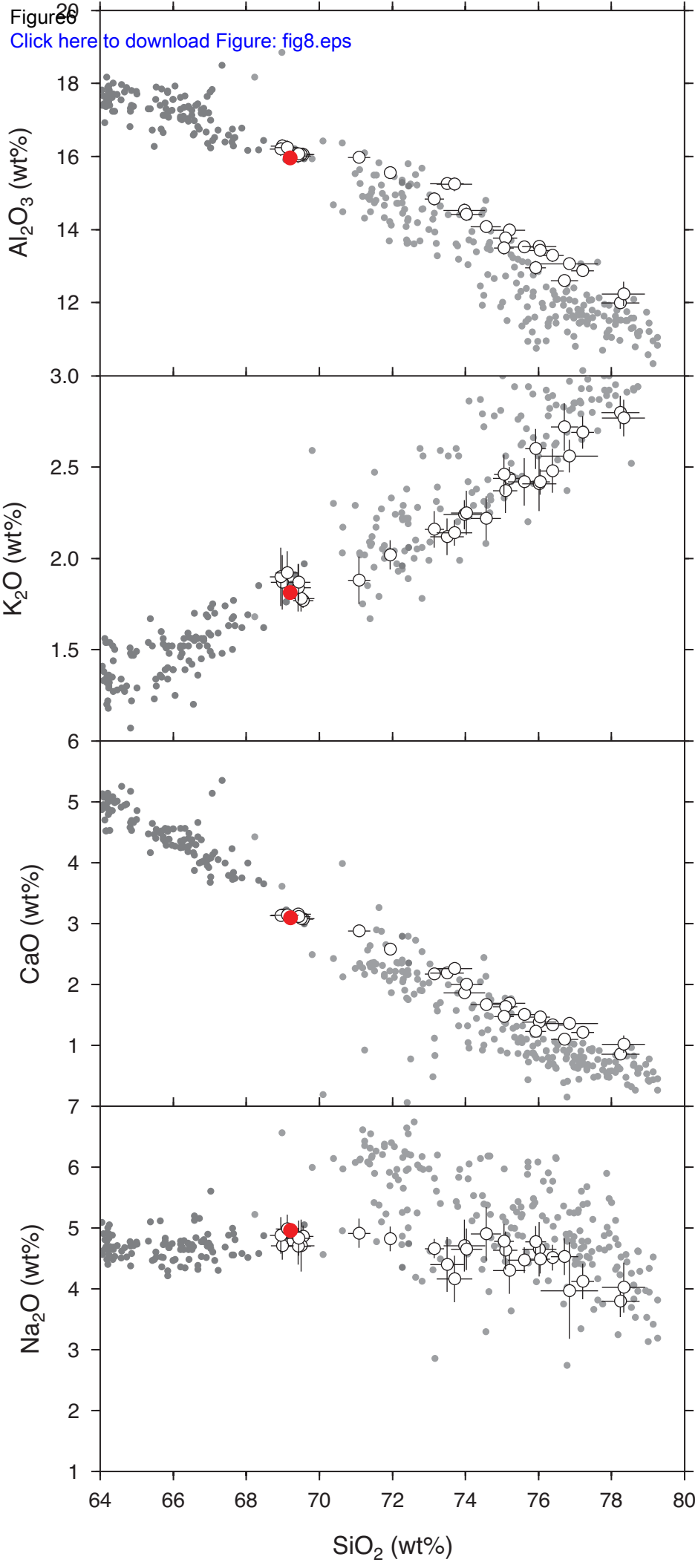

Figure7
Click here to download Figure: fig9_revised.eps

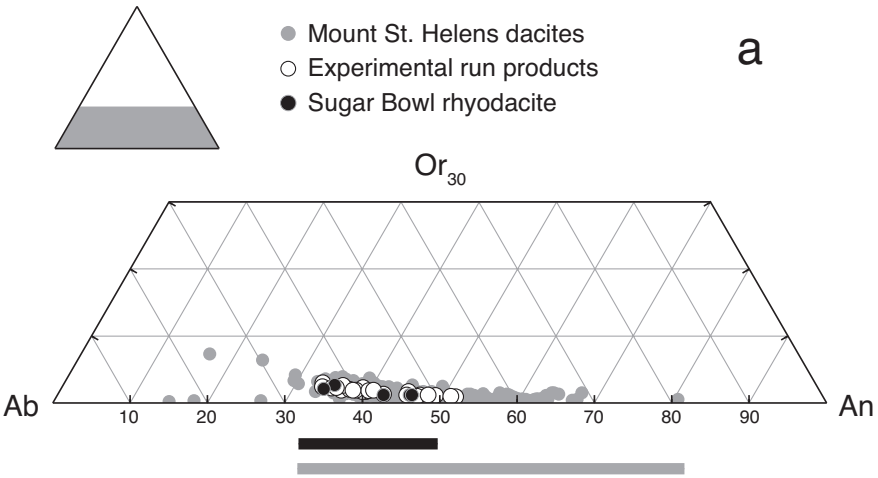

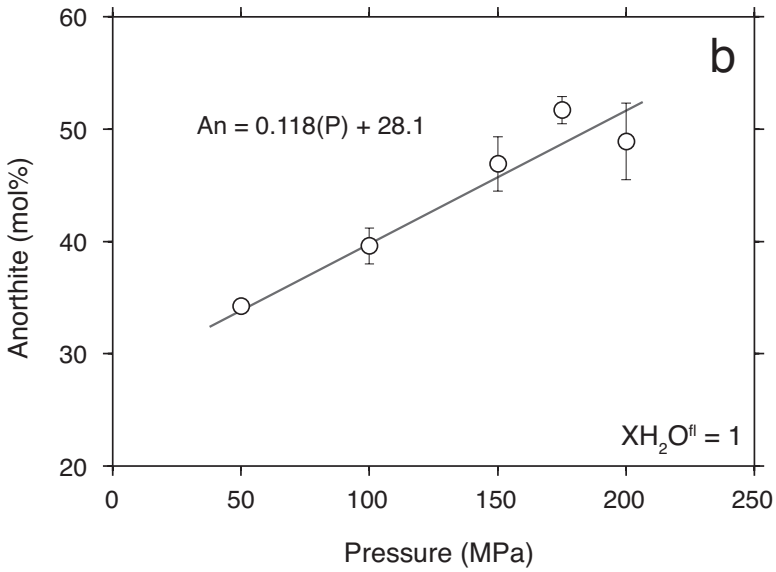

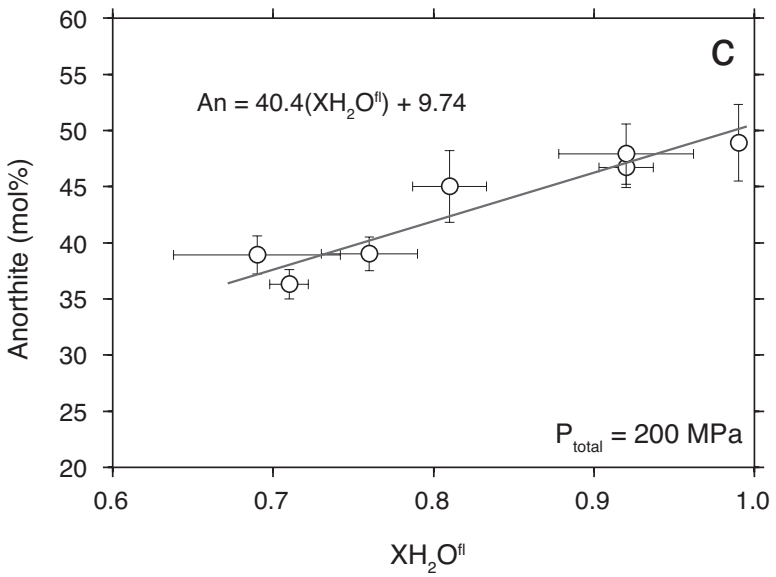

Figure8
Click here to download Figure: fig10_revised.eps

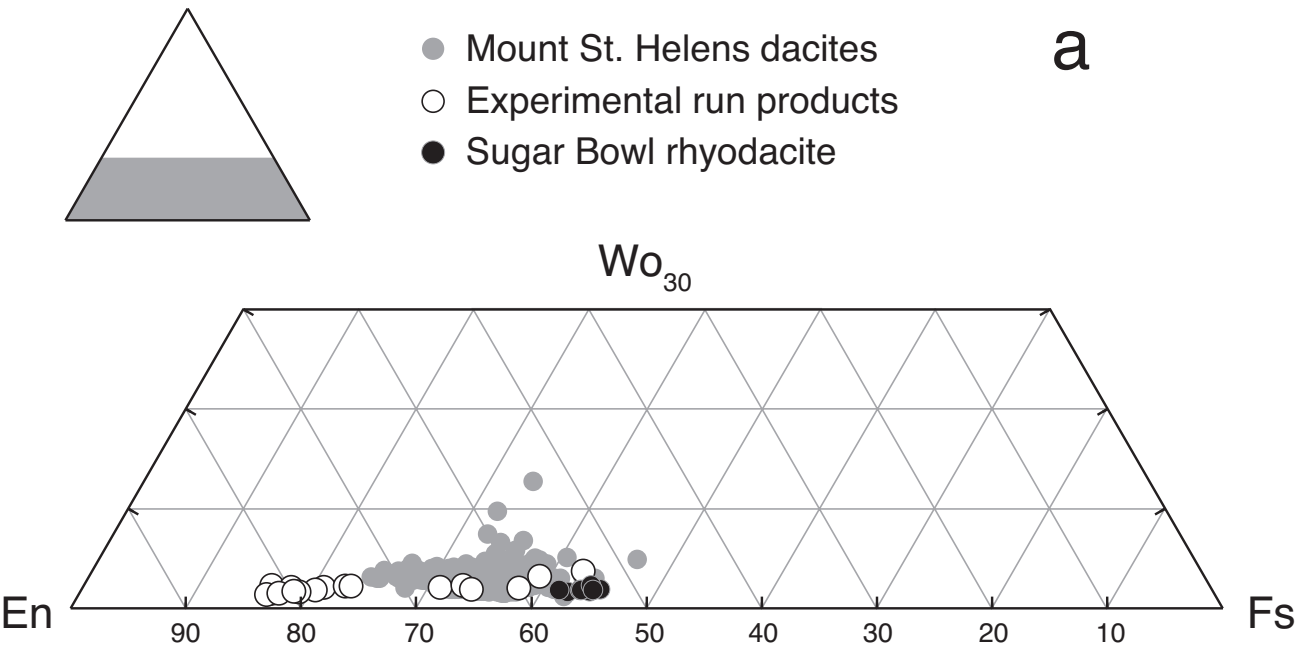

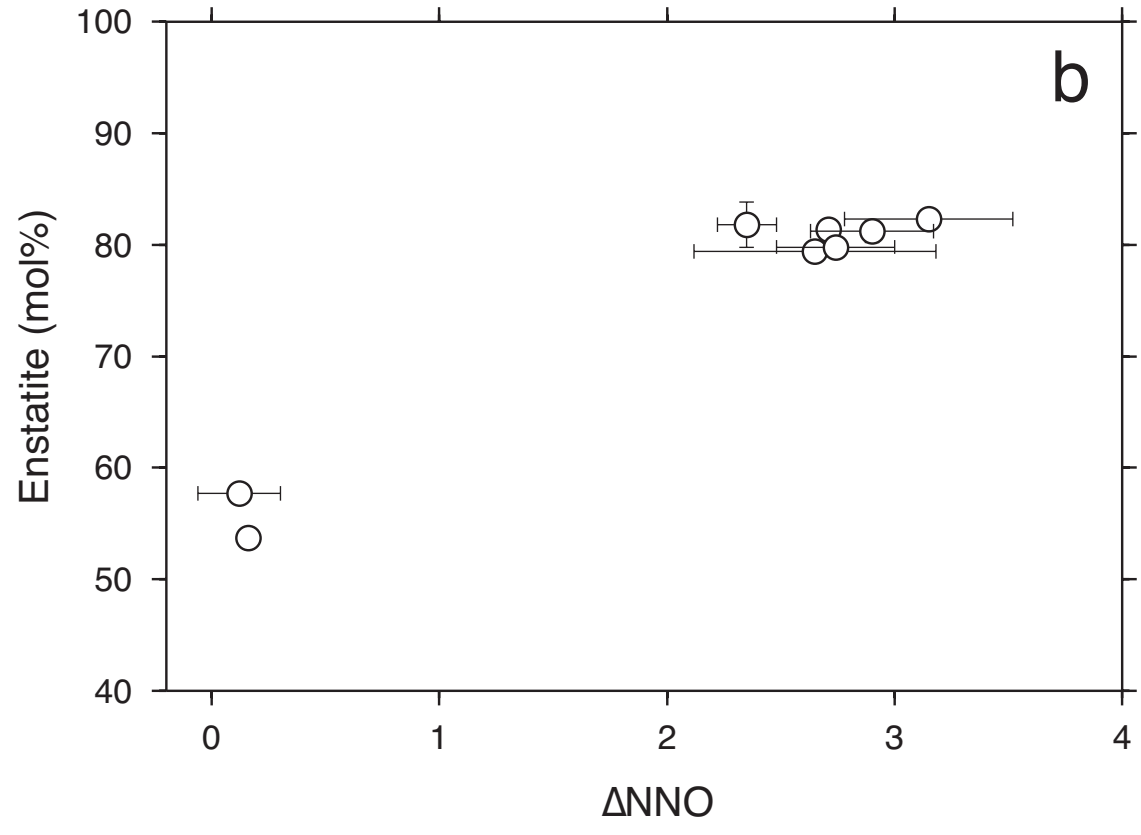

Figure9
Click here to download Figure: fig11_revised.eps

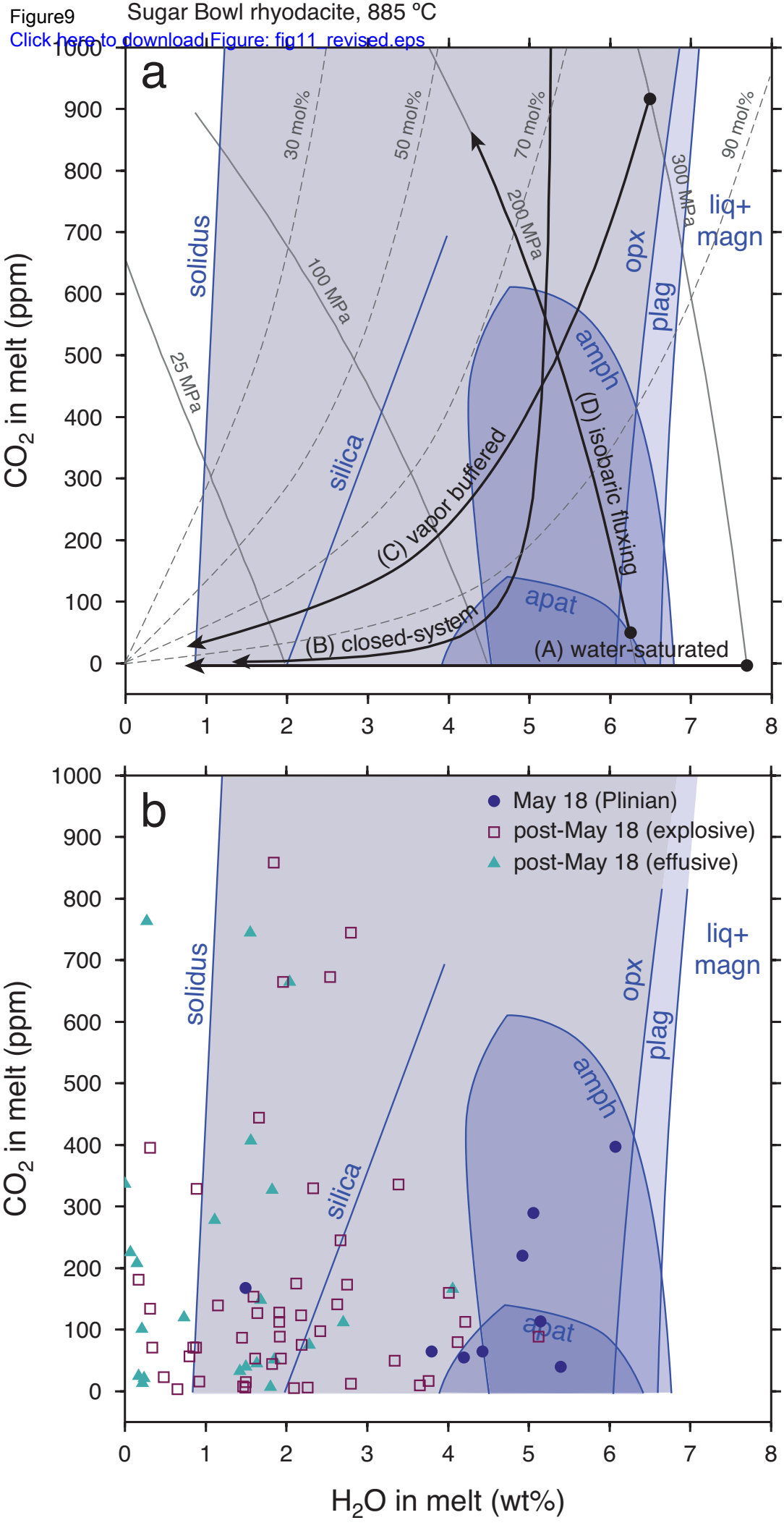

Figure10
Click here to download Figure: fig12.eps

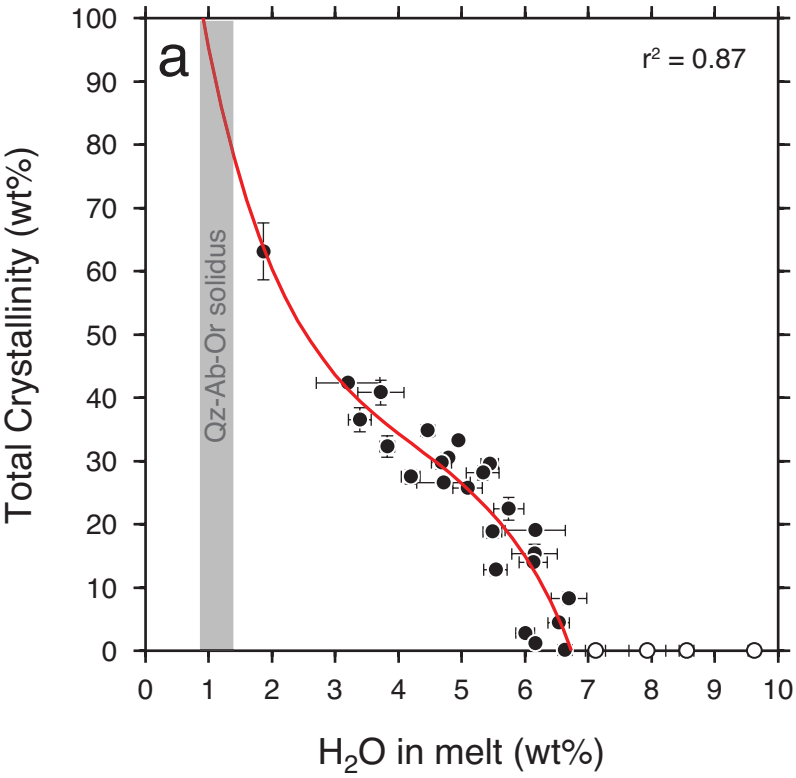

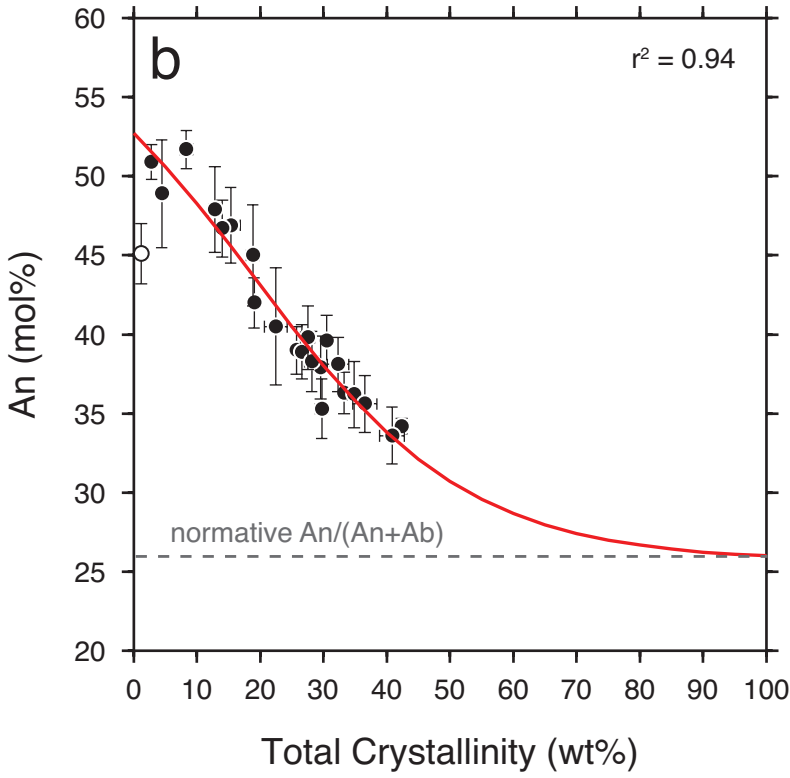

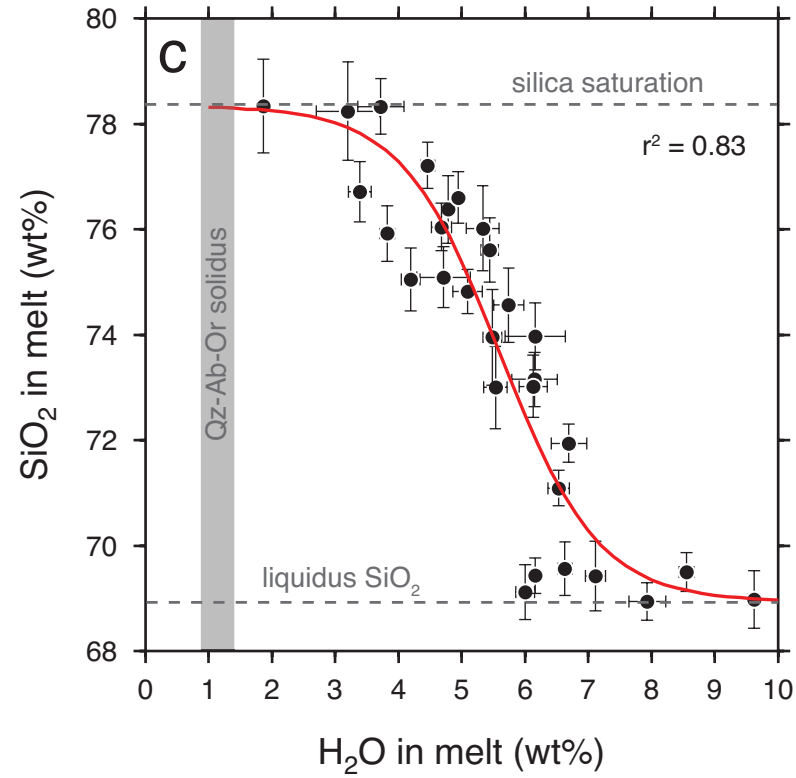

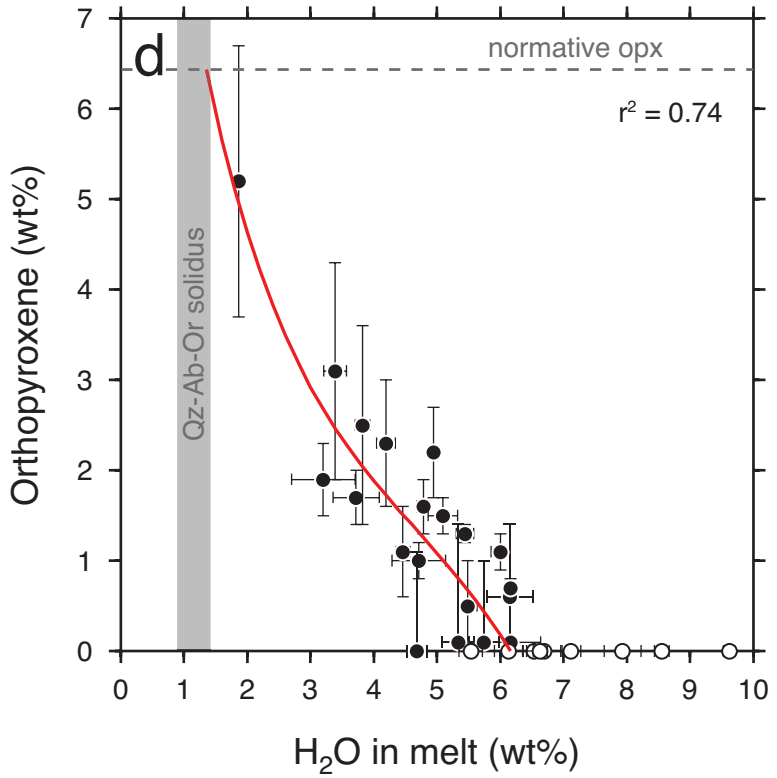

Figure11 Click here to download Figure: fig13.eps

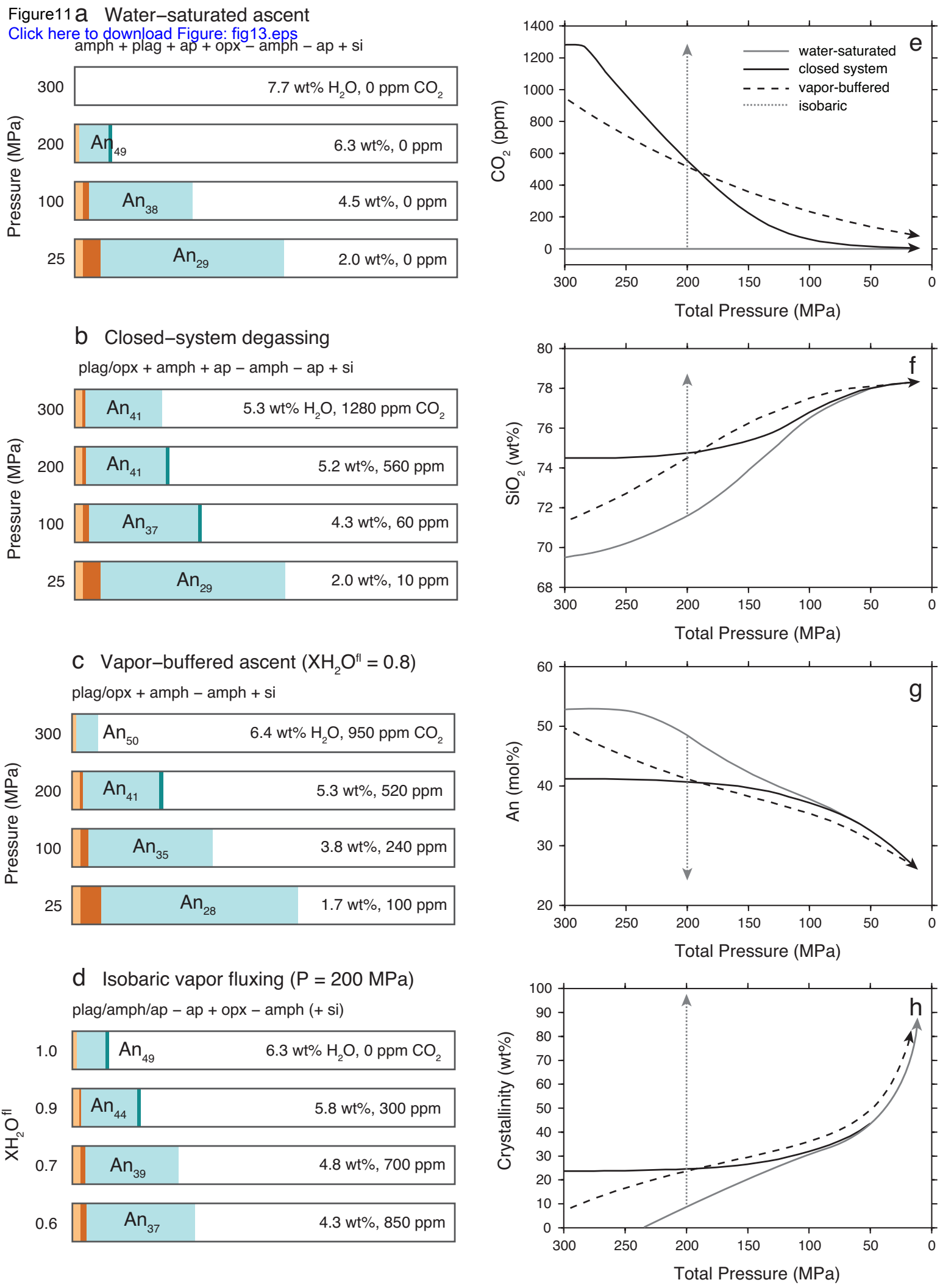

Figure12
Click here to download Figure: fig14_revised.eps

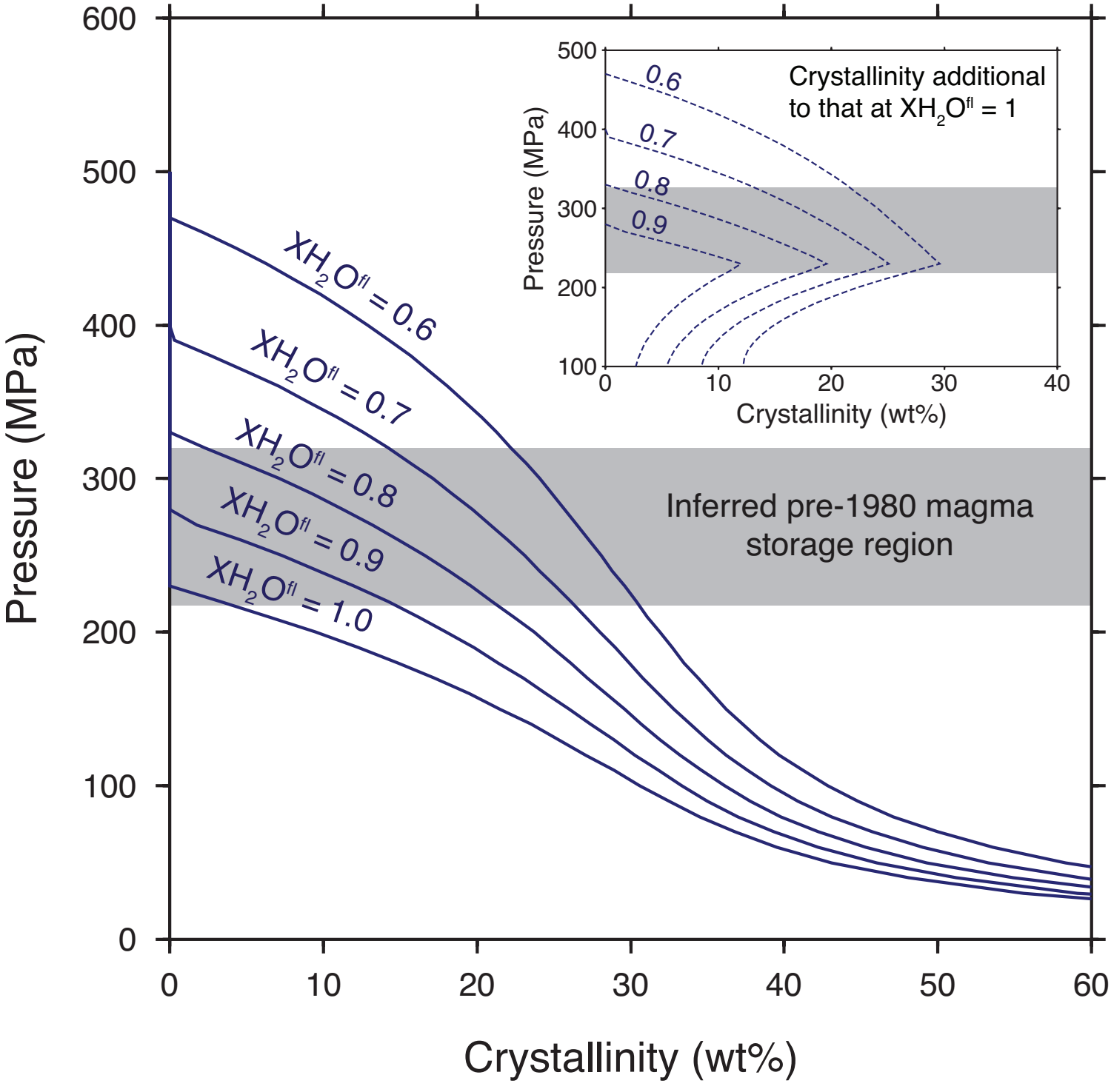

Table1
Click here to download Table: Table1_revised_v2.xls

Table 1 Compositions of experimental starting materials (wt% anhydrous)

	DS-63 [a]	SB3 [b]		SB4 [b]	
SiO_2	69.23	69.52	(0.88)	69.48	(0.54)
TiO_2	0.37	0.36	(0.03)	0.34	(0.03)
Al_2O_3	15.90	16.05	(0.42)	15.93	(0.26)
FeO_T	3.62	3.36	(0.30)	3.58	(0.15)
MnO	0.06	0.06	(0.04)	0.08	(0.05)
MgO	0.83	0.83	(0.06)	0.80	(0.08)
CaO	3.05	3.00	(0.18)	3.02	(0.13)
Na_2O	4.97	4.90	(0.18)	4.88	(0.20)
K_2O	1.86	1.81	(0.08)	1.80	(0.09)
P_2O_5	0.11	0.10	(0.02)	0.10	(0.03)
H_2O [c]	n/a	0.02	(0.00)	0.02	(0.00)
CO_2 [d]	n/a	–	–	0.86	–
CO_2 [e]	n/a	<0.01	(0.01)	1.02	(0.04)
n	n/a	60		60	

Parentheses give 1σ precision of multiple spot analyses
All Fe reported as FeO ("FeO_T")
[a] XRF analysis of Sugar Bowl rhyodacite (Smith and Leeman 1987)
[b] EPMA analysis of starting material fused at 1 atm
[c] SIMS analysis of starting material fused at 1 atm
[d] CO_2 added to starting material
[e] Bulk CO_2 content measured using an ELTRA CS 800 analyzer at Leibniz Universität Hannover.

Table2

Click here to download Table: Table2_revised_v2.xls

Table 2 Experimental run conditions, measured volatile contents, and calculated fluid compositions. All runs at 885 °C.

Sample	P (MPa)	Time (hrs)	H_2O (wt%)		CO_2 (ppm)		XH_2O^{fl} [a]		log $f\ O_2$ [b] (ΔNNO)	CO_2 Source	Run products[c]
Cold-seal pressure vessel experiments (University of Bristol)											
DSB6	200	72	6.53	(0.17)	34	(9)	0.99	(<0.01)	–	n/a	Gl, Pl, Mg, Am
PSB26	175	96	6.69	(0.28)	63	(10)	0.99	(<0.01)	2.7*	n/a	Gl, Pl, Mg, Am
PSB30	150	96	6.15	(0.36)	76	(16)	0.98	(0.01)	–	n/a	Gl, Pl, Mg, Opx, (Am)
PSB32	100	241	4.78	(0.10)	49	(15)	0.97	(0.01)	2.3	n/a	Gl, Pl, Mg, Opx, Ilm, (Ap)
PSB33	50	335	3.20	(0.50)	57	(11)	0.92	(0.02)	–	n/a	Gl, Pl, Opx, Mg, (Ap)
PSB28	25	506	1.86 [d]	–	–	–	1.00 [e]	–	–	n/a	Pl, Gl, Si, Opx, Mg
PSB37	200	216	4.94	(0.03)	700	(32)	0.71	(0.01)	–	$Ag_2C_2O_4$	Gl, Pl, Opx, Mg
PSB42	200	168	5.09	(0.23)	615	(22)	0.76	(0.03)	–	$Ag_2C_2O_4$	Gl, Pl, Mg, Opx
PSB43	200	168	6.13	(0.22)	320	(26)	0.92	(0.02)	–	$Ag_2C_2O_4$	Gl, Pl, Mg, Am
PSB44	175	168	5.44	(0.14)	424	(24)	0.84	(0.02)	–	$Ag_2C_2O_4$	Gl, Pl, Mg, Opx
PSB45	175	168	6.16	(0.48)	234	(22)	0.94	(0.02)	–	$Ag_2C_2O_4$	Gl, Pl, Mg, Am, (Opx)
PSB49	200	96	5.53	(0.19)	318	(18)	0.92	(0.04)	3.4	K_2CO_3	Gl, Pl, Mg, Am, Ilm
PSB50	200	168	5.48	(0.15)	573	(36)	0.81	(0.02)	2.7	K_2CO_3	Gl, Pl, Mg, Opx, (Ilm), (Am)
PSB51	200	168	4.71	(0.42)	724	(10)	0.69	(0.05)	–	K_2CO_3	Gl, Pl, Mg, Opx
PSB52	150	209	5.33	(0.26)	201	(23)	0.91	(0.02)	3.1	K_2CO_3	Gl, Pl, Mg, Am, Ilm, (Opx)
PSB53	150	209	4.46	(0.11)	306	(12)	0.81	(0.01)	2.9	K_2CO_3	Gl, Pl, Mg, Opx, Ilm, (Am)
PSB54	150	209	3.72	(0.36)	437	(81)	0.67	(0.08)	2.6	K_2CO_3	Gl, Pl, Mg, Opx, Ilm, Si
PSB55	100	336	4.19	(0.15)	118	(9)	0.89	(0.02)	–	K_2CO_3	Gl, Pl, Opx, Mg
PSB56	100	336	3.82	(0.12)	197	(9)	0.80	(0.02)	–	K_2CO_3	Gl, Pl, Opx, Mg
PSB57	100	336	3.39	(0.18)	258	(23)	0.71	(0.04)	–	K_2CO_3	Gl, Pl, Opx, Mg
PSB58	225	48	6.63	(0.11)	32	(4)	0.99	(<0.01)	1.2*	n/a	Gl, (Mg)
PSB59	175	167	5.74	(0.24)	248	(7)	0.92	(0.01)	3.0	K_2CO_3	Gl, Pl, Mg, Ilm, (Opx), (Am)
PSB60	175	167	4.68	(0.16)	379	(16)	0.80	(0.02)	2.7	K_2CO_3	Gl, Pl, Mg, Am, (Opx), (Ilm)
Internally-heated pressure vessel experiments (Leibniz Universität Hannover)											
PSB62	350	120	8.55	(0.12)	34	(2)	1.00	(<0.01)	0.9*	n/a	Gl, (Mg)

Sample	P (MPa)	Time (hrs)	H_2O (wt%)	CO_2 (ppm)	$XH_2O^{fl\ a}$	log $f\ O_2$ [b] (ΔNNO)	CO_2 Source	Run products[c]
PSB63	350	120	7.11 (0.16)	1001 (12)	0.85 (0.01)	0.2*	K_2CO_3	Gl, (Mg)
PSB64	350	120	6.00 (0.15)	1408 (26)	0.69 (0.02)	0.1*	K_2CO_3	Gl, Pl, Opx, (Mg)
PSB65	457	120	9.62 (0.09)	63 (5)	1.00 (<0.01)	1.5*	n/a	Gl, (Mg)
PSB66	457	120	7.93 (0.29)	1700 (21)	0.82 (0.02)	0.2*	K_2CO_3	Gl, (Mg)
PSB67	457	120	6.16 (0.09)	2329 (30)	0.60 (0.01)	0.2*	K_2CO_3	Gl, Opx, Pl, (Mg)

H_2O and CO_2 contents of experimental glasses measured by SIMS. Parentheses give 1σ precision of multiple spot analyses.

[a] Calculated mole fraction water in the equilibrium fluid/vapor (Papale et al. 2006)

[b] Log oxygen fugacity relative to the NNO buffer (after O'Neill and Pownceby 1993). Stars indicate values calculated from measured glass Fe3+/ΣFe using tl formulae of Kress and Carmichael (1991). All other values calculated from coexisting cubic and rhombohedral oxide compositions (ILMAT; Lepage 2003) using the oxybarometer of Andersen and Lindsley (1988) and the solution model of Stormer (1983), with temperatures forced to the known run temperature.

[c] Gl: glass, Pl: plagioclase, Am: amphibole, Opx: orthopyroxene, Magn: magnetite–ülvospinel, Ilm: ilmenite–hematite, Si: silica phase, Ap: apatite. Phases listed in order of decreasing abundance. Trace phases in parentheses.

[d] Modeled H_2O solubility from Papale et al. 2006 (experimental glass could not be measured).

[e] Estimated fluid composition (experimental glass could not be measured).

ıe

Click here to download Electronic supplementary material: Riker_et_al_supplementary_information.doc

Click here to download Electronic supplementary material: figS1.eps

Click here to download Electronic supplementary material: TableS1_phase_proportions.xls

Click here to download Electronic supplementary material: TableS2_glass.xls

Click here to download Electronic supplementary material: TableS3_plag.xls

Click here to download Electronic supplementary material: TableS4_other_minerals.xls

Click here to download Electronic supplementary material: Riker_LEPR.xls